



This article appeared in a journal published by Elsevier. The attached copy is furnished to the author for internal non-commercial research and education use, including for instruction at the authors institution and sharing with colleagues.

**Other uses, including reproduction and distribution, or selling or licensing copies, or posting to personal, institutional or third party websites are prohibited.**

**In most cases authors are permitted to post their version of the article (e.g. in Word or Tex form) to their personal website or institutional repository. Authors requiring further information regarding Elsevier's archiving and manuscript policies are encouraged to visit:**

<http://www.elsevier.com/copyright>



# Mineral weathering and elemental transport during hillslope evolution at the Susquehanna/Shale Hills Critical Zone Observatory

Lixin Jin<sup>a,\*</sup>, Ramesh Ravella<sup>a</sup>, Blake Ketchum<sup>a</sup>, Paul R. Bierman<sup>b</sup>, Peter Heaney<sup>c</sup>, Timothy White<sup>d</sup>, Susan L. Brantley<sup>a</sup>

<sup>a</sup> Center for Environmental Kinetics Analysis, Earth and Environmental Systems Institute, The Pennsylvania State University, University Park, PA 16802, USA

<sup>b</sup> Department of Geology and School of Natural Resources, University of Vermont, Burlington, VT 05405, USA

<sup>c</sup> Department of Geosciences, The Pennsylvania State University, University Park, PA 16802, USA

<sup>d</sup> Earth and Environmental Systems Institute, The Pennsylvania State University, University Park, PA 16802, USA

Received 17 June 2009; accepted in revised form 31 March 2010; available online 7 April 2010

## Abstract

Located in the uplands of the Valley and Ridge physiographic province of Pennsylvania, the Susquehanna/Shale Hills Critical Zone Observatory (SSHO) is a tectonically quiescent, first-order catchment developed on shales of the Silurian Rose Hill Formation. We used soil cores augered at the highest point of the watershed and along a subsurface water flowline on a planar hillslope to investigate mineral transformations and physical/chemical weathering fluxes. About 25 m of bedrock was also drilled to estimate parent composition. Depletion of carbonate at tens of meters of depth in bedrock may delineate a deep carbonate-weathering front. Overlying this, extending from ~6 m below the bedrock–soil interface up into the soil, is the feldspar dissolution front. In the soils, depletion profiles for K, Mg, Si, Fe, and Al relative to the bedrock define the illite and chlorite reaction fronts. When combined with a cosmogenic nuclide-derived erosion rate on watershed sediments, these depletion profiles are consistent with dissolution rates that are several orders of magnitudes slower for chlorite ( $1\text{--}5 \times 10^{-17} \text{ mol m}^{-2} \text{ s}^{-1}$ ) and illite ( $2\text{--}9 \times 10^{-17} \text{ mol m}^{-2} \text{ s}^{-1}$ ) than observed in the laboratory. Mineral reactions result in formation of vermiculite, hydroxy-interlayered vermiculite, and minor kaolinite. During weathering, exchangeable divalent cations are replaced by Al as soil pH decreases.

The losses of Mg and K in the soils occur largely as solute fluxes; in contrast, losses of Al and Fe are mostly as downslope transport of fine particles. Physical erosion of bulk soils also occurs: results from a steady-state model demonstrate that physical erosion accounts for about half of the total denudation at the ridgetop and midslope positions. Chemical weathering losses of Mg, Na, and K are higher in the upslope positions likely because of the higher degree of chemical undersaturation in porewaters. Chemical weathering slows down in the valley floor and Al and Si even show net accumulation. The simplest model for the hillslope that is consistent with all observations is a steady-state, clay weathering-limited system where soil production rates decrease with increasing soil thickness.

© 2010 Elsevier Ltd. All rights reserved.

## 1. INTRODUCTION

The Earth's surface comprises a weathering engine that solubilizes and disaggregates rock to form regolith. Regolith formation contributes to important processes such as nutrient cycling, carbon sequestration, erosion, and acid rain mitigation; thus, it is important that we learn to predict

\* Corresponding author. Tel.: +1 814 865 9384.  
E-mail address: [luj10@psu.edu](mailto:luj10@psu.edu) (L. Jin).

the rates and mechanism of such regolith formation. Over the long term, the rates of weathering and erosion also combine to control the evolution of landscapes and define the access, rates of motion, and time scales of water and energy movement within the Critical Zone (CZ) (Stallard, 1992; White et al., 1996, 2001, 2005; Riebe et al., 2003; Amundson, 2004; Heimsath et al., 2005; Brantley et al., 2006; Yoo et al., 2007; Anderson et al., 2007; Brantley and White, 2009). An understanding of the coupled processes that control regolith formation on all important parent lithologies is required to predict how the CZ will change in response to anthropogenic and climate perturbation. To understand such phenomena, watersheds are utilized to investigate intensively the relevant chemical, physical, and biological aspects of weathering on specific lithologies (e.g., White and Blum, 1995; Chadwick et al., 1999; Gaillardet et al., 1999; Jacobson et al., 2003; West et al., 2005; Williams et al., 2007).

As a ubiquitous lithology that covers about 25% of continental land mass (Amiotte-Suchet et al., 2003), shale has been the focus of some pioneering weathering studies (Littke et al., 1991; Kolowith and Berner, 2002; Piereson-Wickmann et al., 2002; Amiotte-Suchet et al., 2003; Copard et al., 2007). However, quantitative models to predict rates of shale weathering are still unavailable. Partly in response to the need for such models, an observatory to study the inter-relationships among hydrology, geochemistry, ecology, and geomorphology has been established at the Shale Hills catchment in central Pennsylvania (hereafter termed the Susquehanna/Shale Hills Observatory or SSHO), developed largely on shale in the Rose Hill Formation. Importantly, Rose Hill Formation represents the oxidized end-member in the continuum of compositions observed for shales worldwide. The full range of shale compositions, including organic-rich endmembers, may be important in determining global fluxes of C, heavy metals and P worldwide (e.g., Petsch et al., 2001; Kolowith and Berner, 2002). The goals of this study are to: (1) identify mineral transformations during weathering of the Rose Hill shale; (2) attribute soil elemental depth profiles to mineral reaction fronts; and (3) use models of hillslope evolution to understand chemical weathering and physical erosion along a planar hillslope. The relatively limited variation in parent lithology at SSHO provides a well-constrained system to investigate relationships among weathering and erosion in a first-order catchment within a tectonically quiescent setting.

## 2. METHODS

### 2.1. Site description

The Susquehanna/Shale Hills observatory is an 8-hectare catchment located within the Valley and Ridge Physiographic Province of the Appalachian Mountains in central Pennsylvania (Fig. 1A). At SSHO, the mean annual temperature is 10 °C and the mean annual precipitation is 107 cm (NOAA, 2007). Within this forested catchment, a 1st-order ephemeral stream within the catchment flows to Shavers Creek, which eventually joins the Susquehanna

River via the Juniata River. The catchment is characterized by a stream channel which is aligned roughly east-west between narrow ridges (Fig. 1A). The average local relief from the valley floor to the ridge top is 30 m and the average channel gradient is 4.5% (Lynch, 1976). The gradients of the south-facing and north-facing slopes are 23° and 28°, respectively.

The geologic structure in the region is characterized by tight plunging folds in Silurian-aged strata. The catchment overlies shales of the Rose Hill Formation of the Clinton Group (Folk, 1960; Lynch, 1976; Lynch and Corbett, 1985). Strike and dip measured on an extremely limited exposure of bedrock at one point along the catchment floor are N54°E and 76°NW, respectively (Fig. 1A). Strike and dip measured stratigraphically and geographically proximal to the catchment range from 60° to 80°. However, borehole televiewer studies near the entrance of the catchment indicate more gentle dips of approximately 25°, consistent with results from three-point calculations on the regional geologic map (Hoskins, 1976). Tight meter-scale kink folds have been observed nearby in the Rose Hill Formation (Rose, 1973). These combined observations suggest that the structural setting below SSHO is complex with gently to steeply dipping and faulted strata. Characteristic erosion rates in the Appalachian Mountain region range from 8 to 29 m/Myrs with northern shale units (e.g., the SSHO) near the lower limit of this range (Roden and Miller, 1989; Blackmer et al., 1994; Reuter et al., 2004).

The 700-foot-thick Silurian-age Rose Hill Formation consists of olive-pink, grayish-buff shales with a few interbedded limestones (Lynch, 1976). Soil thickness, surveyed by augering and ground penetrating radar, averages 1.4 m in the catchment but varies from shallower at the ridge top to much deeper in the valley floor and swales (Lin et al., 2006). Soils show evidence of bioturbation and tree throw (Lin et al., 2006). As delineated by topography, location, soil thickness, and redox features, five soil series have been previously mapped in the catchment (Lin, 2006; Lin et al., 2006; Lin and Zhou, 2008). Soils on the ridge are mapped as Weikert series whereas planar and convex hillslope soils belong to the Berks series. All are loamy-skeletal, mixed, active, mesic Dystrudepts according to the US Soil Taxonomy (Lin and Zhou, 2008).

The SSHO has experienced at least two major perturbations in the geologically recent past: a perturbation from peri-glacial to modern conditions at approximately 15 kya (Gardner et al., 1991), and a perturbation due to clearing of forests during colonial occupation. Extensive data sets are available at SSHO from forestry field experiments: geographic information surveys, 1-m digital elevation model data (DEM), soil moisture synoptic sampling, soil mapping, streamflow monitoring, and preliminary ground penetration radar and gravity measurements from 1996-present (Lynch, 1976; Lynch and Corbett, 1985; Duffy and Cusumano, 1998; Lin et al., 2006; Qu and Duffy, 2007). The site is presently managed as a Pennsylvania State University experimental forest.

To characterize weathering of this catchment, pedons and catenas were chosen to investigate the propagation rates of weathering for sites representing different patterns

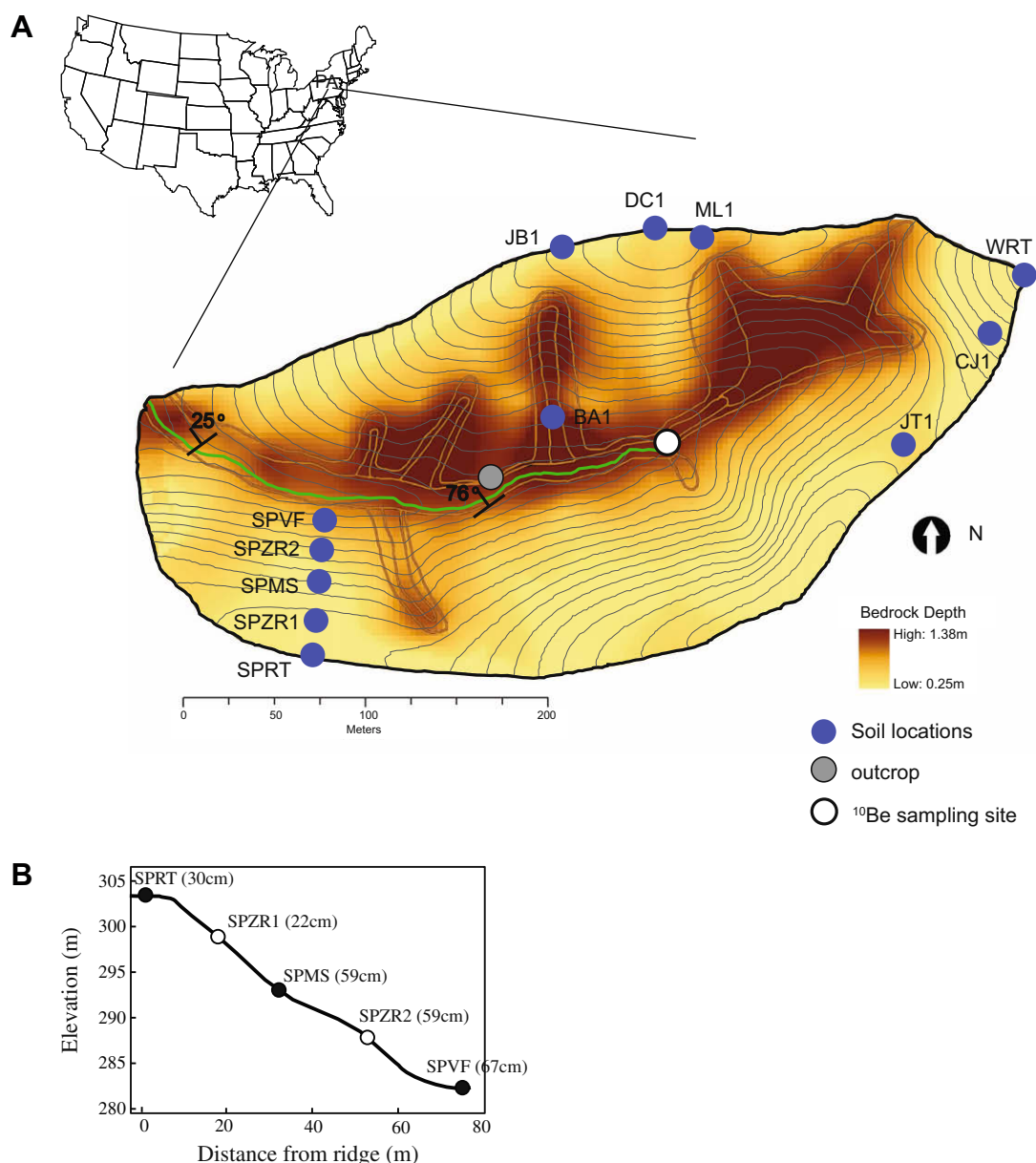


Fig. 1. Soil sampling locations in the Shale Hills catchment (A; modified from Lin et al., 2006). Background color indicates soil thickness. DC1 is the drill core site, where 25 m of parent shale was sampled as chips and powder. Soil core WRT represents the 1D site. Soil cores SPRT (SPRT2), SPMS (SPMS2) and SPVF (SPVF2) comprise the 2D planar transect. Two more cores are sampled along the 2D transect for bulk density analysis (SPZR1 and SPZR2). The strike and dip were measured from an outcrop (grey circle) and near the entrance. Five other cores were collected as shown in other sites of the SSHO and chemically analyzed for the deepest sample to constrain the parent composition. One stream sediment was collected near the headwater of the stream (white circle) and analyzed for meteoric  $^{10}\text{Be}$  to estimate erosion rates. (B) Cross section of the planar transect illustrates shape of the hillslope. Numbers in parentheses are soil thickness in centimeters. Notice that the hillslope is flat at SPRT, concave at SPVF, and planar at SPMS.

of sediment erosion, accumulation and water flow. These sites were selected where subsurface fluid flow in the regolith is largely one-dimensional (“1D”) and vertical (ridge top), two-dimensional (“2D”) downslope (planar hillslope), and three-dimensional (“3D”) downslope (convergent hillslope, swale). The overall strategy of the approach is to quantify weathering rates at each of these types of sites in order to integrate patterns over the entire watershed. In recognition of the effects of aspect as well as underlying

geological structure, two 2D and two 3D sites were each identified in the catchment, one on the north-facing slope and one on the south-facing slope.

The 1D-weathering site comprises the highest point in the catchment. Due to its location, this site does not include the effects of sedimentation but only losses through weathering and erosion. Interpretation of weathering at this site follows the approach described previously in the literature for other such 1D sites (Murphy et al., 1998; White et al.,



2001). In contrast to the 1D-site, the 2D- and 3D-weathering sites include not only the effects of propagation of the weathering front but also the effects of downslope regolith transport, i.e., the sites experience input/output of sediments and thus require more complex models for weathering (Yoo et al., 2007; Burke et al., 2007; Green et al., 2006). In this paper, we focus on chemical and mineralogical observations for the 1D site and the 2D planar hillslope (catena) on the southern slope (north-facing).

## 2.2. Drill core

Using a rotary air drill, we drilled 25 m deep into bedrock at the northern ridge and recovered disaggregated shale chips (site labeled as DC1 on Fig. 1A). Chips were used to characterize parent shale. Due to the steep dip of the bedding inferred from the outcrop at the valley floor, these samples may only correspond to about 6 m of the Rose Hill Formation. Soil samples (labeled DC1-1 (depth from surface = 0.18 m) and DC1-2 (depth from surface = 0.3 m)) were also collected at this location before drilling.

A rough estimate of the bulk densities of rock chips from drilling was determined by weighing chips dry and then measuring volume by displaced water using a graduated cylinder. Grain densities of representative DC1 samples were also measured with higher sensitivity using a pycnometer after grinding the samples to fine particles using a shatter box.

## 2.3. Augered soil cores

Soil profiles were sampled at SSHO using a 2-in. diameter auger. In this study, “soil” is operationally defined to be all regolith that can be sampled with a hand auger until the point of refusal. The zero depth was defined as the bottom of the organic layer or, equivalently, the top of the mineral soil. For each soil sample, an interval of about 10 cm was collected but the sample itself is labeled by the mid-point of this depth range.

One profile at the highest point of the catchment (WRT) was chosen as the 1D site (Fig. 1A). A roughly planar hillslope in the south side of the catchment was chosen as the southern 2D catena site (Fig. 1B). Duplicate soil profiles were collected at three sites down this hillslope: the South Planar Ridge Top (SPRT, SPRT2), Middle Slope (SPMS, SPMS2) and Valley Floor (SPVF, SPVF2) (Fig. 1). The two profiles at each location were only a few meters apart at the same elevation along the hillslope: one was characterized extensively while the other analyzed for chemistry only. Sample site SPVF is located ~5 m from the stream, i.e., in the footslope. Thus, the water table and the redox conditions in the deeper soil fluctuate seasonally.

We also report the chemistry of the bottom-most samples from five other soil profiles (BA1, JB1, ML1, CJ1, JT1) collected throughout the SSHO (Fig. 1A). These relatively unweathered materials were used to evaluate the heterogeneity of the parent shale as discussed further below.

Grain densities of representative weathered soil samples were measured with a pycnometer. Two more cores (SPZR1 and SPZR2, Fig. 1A and B) were also collected along the

planar hillslope for bulk density measurement following the method of Blake and Hartge (1986). For these, we used a sampler of known volume attached to our auger. Samples were then transferred to polyethylene bags, dried at 105 °C in the laboratory, and weighed after drying. Bulk density was computed using the known volume of the sampler and the mass after drying.

## 2.4. Sample preparation and elemental analysis

Soil pH values were measured in a slurry of soil and deionized water (1:1) (USDA, 2004). The remainder of each sample was air-dried immediately after sampling, homogenized and stored in resealable bags. Bulk samples, including rock fragments, were ground to pass through a 100-mesh sieve (<150 µm). Elemental abundances were measured by SGS Canada Inc. (Minerals Services Laboratory at Toronto, Ontario; method ICP95A). In this analysis, 1 g of ground sample was combusted at 950 °C for 1 h, and the difference in sample weight before and after combustion was reported as loss on ignition (LOI). The samples were further fused with lithium metaborate at 950 °C and re-dissolved in dilute nitric acid. Resultant solutions were analyzed by inductively coupled plasma optical emission spectrometer (ICP-OES) for major elements and inductively coupled plasma mass spectrometer (ICP-MS) for Zr. All analyses reported here are estimated to have precision of ±3%. Soil samples from WRT, SPZR1, SPZR2, SPRT2, SPMS2 and SPVF2 were analyzed at the Materials Characterization Laboratory (MCL) of Pennsylvania State University using the same lithium metaborate fusion method but without measuring LOI and then analyzed using ICP-OES for major elements. To investigate rock fragment chemistry in one location, elongated centimeter-sized shale chips from three depths of the augered SPRT core were also analyzed for elemental chemistry at Penn State. An inter-laboratory comparison was performed by running two standard reference materials (soils SRM2709 and SRM2711 from NIST) at SGS and MCL for major elements. The chemistry data by the two laboratories are within reasonable ranges of the certified values (Appendix Table 1).

## 2.5. Separation of clay fraction

For some samples, clay fractions were separated from bulk soils following the method of White and Dixon (2003) and Poppe et al. (2002). To start, 15–30 g of sample was weighed into a 250-ml glass beaker. A dilute acetic acid solution was prepared (1:4 acid to water ratio) and 50–75 ml portions were added to the samples to remove carbonate minerals. The sample and acid mixture were allowed to react for 2 h and additional 50 ml aliquots of acid was added and left to react overnight. Supernatant was decanted without loss of sample. A 3% H<sub>2</sub>O<sub>2</sub> solution was prepared and 50–75 ml aliquots were added to each sample. Samples were then heated and maintained for 30 min below 100 °C to facilitate oxidative removal of any organic matter in the samples. An additional 10 ml of 30% H<sub>2</sub>O<sub>2</sub> was added to samples rich in organic matter along with 50 ml of 3% H<sub>2</sub>O<sub>2</sub> to all the samples until frothing subsided. These solutions were transferred to 250-ml Teflon bottles

and centrifuged at 2000 rpm for 5 min. Supernatant was decanted and the soil was transferred into wide-mouthed 1-L glass bottles using distilled water. A small quantity (about 10 mg) of sodium hexametaphosphate dispersant was added to each sample and bottles were filled with distilled water to a height of ~10 cm. The bottles were shaken vigorously, then magnetically stirred for 20–30 s.

After stirring, the bottles were allowed to settle for 3 h 50 min at 22 °C so that only clay fractions remained suspended. Supernatant from the top 5 cm was then removed using a syringe. Successive extractions of clay fraction were accomplished by re-suspending the samples in distilled water. After each suspension, the supernatant was collected: this process was repeated until the solution in the top 5 cm was clear, indicating that the entire clay fraction was removed. The solutions were collected in 250-ml beakers and dried at 60 °C. After oven drying, samples were ground to fine powders using a mortar and pestle and stored in air-tight glass bottles for further analysis.

## 2.6. XRD and SEM analysis

Minerals in DC1 samples, selected soils, and in the clay fraction of soils were identified using X-ray diffraction (XRD). Samples were mounted onto a holder by a side loading technique (Moore and Reynolds, 1997) to achieve random orientation. Using a Scintag PAD-V powder X-ray diffractometer, samples were scanned from 2° to 70° 2 $\theta$  at 35 kV voltage and 30 mA current with Cu-K $\alpha$  radiation ( $\lambda$  = 1.54178 Å) and a Ge solid state detector. Diffraction patterns were collected with a step size of 0.020° 2 $\theta$  at 1° 2 $\theta$  per minute. XRD patterns were analyzed using JADE software.

In addition to mineral identification, mineral abundances were also quantified for selected DC1, SPRT, SPMS, and SPVF bulk samples. XRD patterns were obtained and analyzed using the USGS program RockJock (Eberl, 2003).

Because chemical and thermal treatments can shift clay peaks in XRD patterns allowing differentiation of individual clay minerals, sample clay fractions were further treated sequentially by (i) Mg-saturation with 1 N MgCl<sub>2</sub> solution; (ii) Mg-saturation followed by treatment with ethylene glycol; (iii) K-saturation with 1 N KCl solution; (iv) K-saturation followed by heat treatments at 400 °C and 550 °C, respectively (complete methodologies are summarized in Moore and Reynolds (1997) and White and Dixon (2003)). Slides were prepared at room temperature by spreading powdered samples on zero-background quartz slides with a drop of water and then were left to dry. XRD patterns were obtained for each sample following treatments (i) through (iv).

A few samples from the DC1 core were also placed on conductive sample holders for observation with FEI Quanta 200 Environmental scanning electron microscopy (SEM).

## 2.7. Cation exchange characterization

To define the clay mineralogy and occupancy of cations in the interlayers, a cation exchange experiment was carried out following the methods of Amacher et al. (1990) and

White et al. (2005). Specifically, representative DC1 and bulk soil samples were sieved so that only particles less than 2 mm were analyzed. About 2.5 g of a sample were weighed into a 50-ml centrifuge tube and 25 ml of 0.1 M BaCl<sub>2</sub>–0.1 M NH<sub>4</sub>Cl solution was added. Samples were shaken for 15 min at 180 oscillation/min, then centrifuged at 2500 rpm for 20 min. The solution was filtered, weighed and analyzed by ICP-OES for major elements at MCL of the Pennsylvania State University. ICP standards were prepared in 0.1 M BaCl<sub>2</sub>–0.1 M NH<sub>4</sub>Cl solution to ensure matrix matching.

Soil residue was washed with de-ionized water, and 10 ml of 4 M acetic acid was added to dissolve carbonate minerals if present (Jacobson et al., 2003). The mixture was shaken for 6 h at 180 oscillation/min, then centrifuged at 2500 rpm for 20 min. The solution was filtered, weighed, and analyzed by ICP-OES for major elements at MCL of the Pennsylvania State University.

## 2.8. Stream water samples

Stream water was sampled near the mouth of the SSHO catchment from October 2006 to October 2008 (approximately 25 samples). Samples were filtered through 0.45  $\mu$ m Nylon syringe filters, and then acidified with a few drops of high purity HNO<sub>3</sub> for cation analysis. Measurements were completed for Ca, Mg, K, Na, Al, Si, and Fe using ICP-OES at MCL of the Pennsylvania State University.

## 2.9. Sampling and characterization of stream sediment for meteoric <sup>10</sup>Be

To estimate a catchment-specific rate of erosion, meteoric <sup>10</sup>Be was extracted from a sample of fluvial sediment (sand fraction) collected from the channel of the ephemeral stream (Fig. 1A). The sediment was powdered and 0.499 g of the powder, along with 299  $\mu$ g of SPEX <sup>9</sup>Be carrier, was processed using the method of Stone (1998) at the University of Vermont and analyzed at Lawrence Livermore National Laboratory using accelerator mass spectrometry. The <sup>10</sup>Be/<sup>9</sup>Be ratio of a full process blank was subtracted from the measured sample ratio.

# 3. RESULTS

## 3.1. Parent shale

At the DC1 site (Fig. 1A), the soil is very shallow (~0.1 m); thus, all samples deeper than 0.1 m at this site are shale bedrock. These DC1 samples were mostly olive or olive grey in color. However, two grey samples (the deepest two samples from 23 m and 24.5 m, respectively) and one olive brown sample at 4.5 m depth were observed. Loss on ignition (LOI) of the DC1 samples averaged 6 wt. %, but was higher at the shallow depths, at ~4.5 m, and also in the bottom-most sample.

DC1 samples (Table 1; Fig. 2A) are generally constant in elemental concentration except for the olive grey sample that showed very high Fe and low Al content at ~4.5 m

Table 1

Elemental concentrations of drill core samples from Shale Hills catchment (DC1-longitude: W077°54.241'; latitude: N40°39.948').

Sample number	Depth range (m)	LOI (%)	Al (%)	Ca (%)	Fe (%)	K (%)	Mg (%)	Mn (%)	Na (%)	P (%)	Si (%)	Ti (%)	Zr (ppm)
DC1-1	0–0.18	7.20	10.43	0.11	5.08	3.41	0.78	0.12	0.40	0.07	27.02	0.68	204
DC1-2	0.18–0.30	6.88	11.96	0.29	5.66	4.24	0.96	0.06	0.33	0.27	27.25	0.70	152
DC1-3	0.30–0.49	7.14	10.80	0.13	5.47	3.64	0.87	0.18	0.36	0.07	26.08	0.65	165
DC1-4	0.49–0.61	6.40	10.69	0.14	5.36	3.65	0.86	0.09	0.27	0.07	26.79	0.67	171
DC1-5	0.61–0.79	6.17	10.74	0.14	5.44	3.74	0.92	0.05	0.44	0.05	26.93	0.65	194
DC1-8	1.1–1.2	6.13	11.33	0.14	5.44	3.98	0.92	0.05	0.42	0.06	26.83	0.67	179
DC1-11	1.5–1.7	6.84	10.90	0.11	5.60	3.69	0.86	0.09	0.30	0.06	26.88	0.66	186
DC1-14	2.4–2.6	5.83	10.69	0.12	5.57	3.73	0.92	0.06	0.50	0.06	26.79	0.65	195
DC1-17	3.4–3.5	5.81	10.32	0.11	5.46	3.63	0.90	0.05	0.36	0.04	25.94	0.62	173
DC1-20	4.3–4.5	7.68	9.16	0.14	12.17	2.47	1.03	0.64	0.37	0.07	24.40	0.52	171
DC1-23	5.2–5.4	5.63	9.84	0.11	5.26	3.46	0.89	0.05	0.33	0.05	26.55	0.61	203
DC1-26	6.1–6.3	5.84	11.06	0.11	5.97	3.93	1.05	0.09	0.28	0.06	27.25	0.67	172
DC1-29	10.7–10.9	6.11	11.01	0.09	5.67	3.88	0.95	0.10	0.36	0.05	26.97	0.63	170
DC1-32	15.2–15.4	5.73	10.58	0.11	5.42	3.88	1.10	0.08	0.35	0.05	26.41	0.57	172
DC1-35	19.8–20.0	5.57	11.01	0.13	5.36	3.95	1.12	0.02	0.32	0.04	26.93	0.62	155
DC1-37	22.9–23.0	5.29	10.74	0.48	5.20	3.87	1.29	0.05	0.37	0.05	26.37	0.58	153
DC1-38	24.4–24.6	8.16	7.73	1.85	5.85	2.60	1.33	0.19	0.28	0.05	27.67	0.46	231
Average <sup>a</sup>			10.75	0.12	5.50	3.76	0.95	0.08	0.36	0.06	26.70	0.64	178
Standard deviation <sup>b</sup>			0.38	0.02	0.19	0.16	0.09	0.04	0.07	0.01	0.38	0.03	14

The average values are used as the chemical composition of the parent shales for  $\tau$  calculations.

LOI and oxides for each sample add up to about  $100 \pm 2\%$ .

<sup>a</sup> Average of elemental concentrations, for samples between 0.30 and 20.0 m excluding 4.3–4.5 m.

<sup>b</sup> Standard deviation of elemental concentrations, for samples between 0.30 and 20.0 m excluding 4.3–4.5 m.

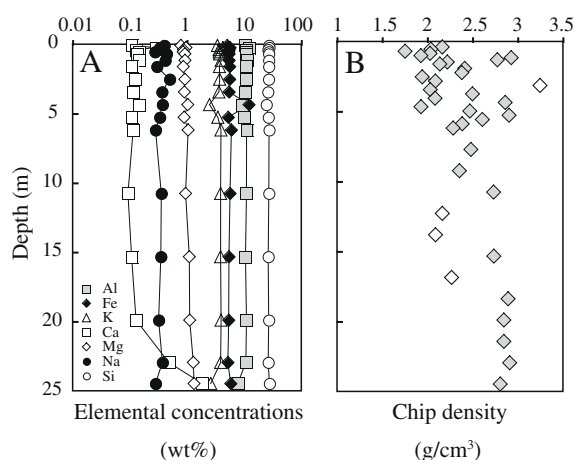


Fig. 2. Major element concentrations (A) and bulk density (B) measured in the 25-m drill core at DC1 site. A relatively high Fe content is observed at 4.5 m depth, above which a large variation in bulk density is also observed. Below 18 m, shale chips recovered from the drill core are smaller, and bulk density is almost constant. The bottom two samples are high in Fe, Ca and Mg, due to the presence of ankerite.

(Fe and Al values differed by more than  $1\sigma$  from the mean of the DC1 data). In addition, the two deepest grey samples are characterized by relatively high concentrations of Ca, Fe and Mn but lower concentrations of K and Al, i.e., these concentrations are more than one standard deviation higher than the mean of the DC1 sample set.

The average composition of shale bedrock was calculated to determine an inferred parent material composition

by averaging the concentrations of DC1 samples between 0.3 m and 20 m, excluding the topmost two soil samples, the sample at 4.5 m, and the deepest two samples. To assess heterogeneity of this parent material, the standard deviation around the mean was calculated: the values ranged from 0.01 to 0.38 wt.% for major elements to about 14 ppm for Zr (Table 1). The standard deviations are observed to be relatively low for elements present at more than 3 wt.% but much higher for elements present at less than 1 wt.%. The average compositions of the deepest, least weathered soils from five cores (BA1, CJ1, ML1, JB1, JT1) were also observed to be similar to the parent material within  $\pm 1\sigma$  (Table 1 and Appendix Table 2). Based on these observations, the averaged DC1 composition (where some samples were excluded as defined above) was used as the composition of the parent material for the following discussion.

Quantitative XRD of several parent samples (DC1) show that the analyzed section of Rose Hill shale is composed predominantly of illite (58 wt.%), quartz (30 wt.%), “chlorite” (either chlorite itself or a mineral exhibiting the same XRD peaks as chlorite; 11 wt.%), and trace amounts of feldspar (plagioclase and K-feldspar) and Fe-oxides (magnetite and hematite) (Table 2). “Chlorite”, as determined from quantitative XRD, is a term that here encompasses chlorite, vermiculite, hydroxy-interlayered vermiculite (HIV), and/or mixtures of these phases (Moore and Reynolds, 1997). Ankerite (Fe- and Mn-rich carbonate) was identified in the two deepest samples (1.4 wt.% and 7.1 wt.%, respectively), consistent with the higher Fe, Mn, Ca and LOI contents and the grey color of those samples. However, carbonate minerals were absent in all shallower samples.

Table 2  
Mineralogy of Shale Hills bedrock and soils, with corresponding  $\tau_{Zr,j}$  values.

Sample and depth (cm)	Quartz		Illite		Chlorite		Fe-oxides	Peat	Disordered kaolinite	Carbonate	Feldspar (wt.%)	Quartz/Zr <sup>b</sup>
	wt.%	$\tau_{Zr,j}$	wt.%	$\tau_{Zr,j}$	wt.%	$\tau_{Zr,j}$	wt.%	wt.%	wt.%	wt.%		
SPRT 0–10	49.9	0.02	29.6	−0.62	5.5	−0.55	2.5	9.8	2.8	—	4.2	0.18
SPRT 20–30	55.7	0.15	30.1	−0.61	8.1	−0.32	2.0	3.6	0.5	—	5.0	0.23
SPMS 0–10	55.1	−0.20	25.4	−0.77	4.8	−0.72	2.1	9.8	2.7	—	5.2	0.16
SPMS 20–30	60.7	0.05	26.7	−0.71	6.1	−0.58	1.9	3.2	1.4	—	6.6	0.21
SPMS 50–59	53.6	0.02	35.5	−0.58	7.1	−0.46	1.7	1.3	0.9	—	5.6	0.20
SPVF 0–10	63.3	−0.08	22.6	−0.80	3.5	−0.79	1.9	7.7	0.9	—	6.2	0.18
SPVF 30–40	43.4	0.01	47.5	−0.31	8.3	−0.23	0.4	0.0	0.4	—	2.8	0.20
SPVF 60–67	36.3	−0.03	54.4	−0.10	9.3	0.00	0.0	0.0	0.0	—	1.2	0.19
DC1-17	30.5		60.8		5.9		2.1	—	—	0	0.3	0.18
DC1-26	30.1		60.3		6.9		1.6	—	—	0	0.5	0.18
DC1-30	31.7		57.1		10.1		0.4	—	—	0	0	—
DC1-37	29.8		55.6		12.2		0	—	—	1.6	0	0.19
DC1-38	45.8		36.0		9.2		0.2	—	—	7.8	0.2	0.20
Average <sup>a</sup>	33.6		54.0		8.8							
Standard deviation <sup>a</sup>	6.9		10.3		2.5							

<sup>a</sup> Averaged from five drill core samples, and used as the parent shale mineralogy for  $\tau_{Zr,j}$  calculation.

<sup>b</sup> Quartz (in %) to Zr (ppm) ratios of bedrock and soils are close, indicating the immobile nature of both phases.

Under SEM, bedrock samples showed relatively homogeneous clay particle morphologies. Most grains appeared to be aggregates of individual particles. Using energy dispersive X-ray analysis (EDX), qualitative chemical analysis was completed. Most samples contained some Fe. EDX analysis was consistent with Fe oxides, clays, and occasional feldspar and zircon grains.

The grain densities of the DC1 chip samples average  $2.62 \pm 0.08 \text{ g/cm}^3$  ( $1\sigma$ ,  $n = 6$ ). The bulk densities determined for chips in the upper 4.5 m show high variability from 1.8 to 3.3  $\text{g/cm}^3$ . In contrast, from 4.5 to 18 m depth, the densities only vary between 2 and 2.8  $\text{g/cm}^3$ . Rock chips (generally several centimeters in dimension) recovered during drilling were also observed to be larger in the upper 17 m compared to deeper samples. Below 18 m, the bulk densities are consistently 2.8–2.9  $\text{g/cm}^3$  (Appendix Table 3 and Fig. 2B). Bulk density can only be greater than grain density if material is lost during measurement. We conclude that some Fe oxides may have been lost during grinding for grain density measurement; furthermore, the bulk density measurements can only be seen as rough values. Despite this, a general trend is observed that chip density increased with depth.

### 3.2. Soils

Soil thickness varies significantly among the studied locations, depending on elevation and topographic features. Soils near the ridge tops are thin (WRT, SPRT, DC1, JB1, ML1), varying from 20 cm at DC1 and WRT to 30 cm at SPRT, 40 cm at JB1 and 28 cm at ML1. At DC1 and WRT, broken shale chips lie within the organic layer and are occasionally visible on the ground surface. Along the 2D-planar transect, soil thickness increases downslope from 30 cm at the ridge top (SPRT) to 59 cm at the middle slope (SPMS) and 67 cm at the valley floor (SPVF) (Fig. 1B).

Although the hillslope is nonconvergent and thus largely planar when considered along the east-west axis of the SSHO channel, when considered along a downslope axis, it is slightly convex at the ridgetop (SPRT) and slightly concave at the footslope position, SPVF.

Soil pH, ranging from 3.5 to 5.0, generally increases with depth, except for the ridge top site where pH is nearly constant at  $\sim 4$  (Table 3). The bulk density of soils increases from less than 1.0  $\text{g/cm}^3$  in the organic-rich surface soils to about 1.8  $\text{g/cm}^3$  in the deepest soil, where it is similar to shallow drill core samples (Appendix Table 3 and Fig. 3A). The grain densities of soil samples average  $2.63 \pm 0.05 \text{ g/cm}^3$  ( $1\sigma$ ;  $n = 5$ ), similar to that of the parent shale ( $2.60 \pm 0.08 \text{ g/cm}^3$ ) ( $1\sigma$ ;  $n = 6$ ), except for the topmost soil (0.69  $\text{g/cm}^3$ ), which contains significant amounts of organic matter (Appendix Table 3).

The minerals in the parent shale dominate the mineralogy of all the bulk soil samples, with addition of kaolinite (0–3 wt%) and organic matter (Table 2). Detailed clay characterization confirms the absence of smectite and the presence of kaolinite in the soil clay fractions. Kaolinite is inferred to be a secondary phase because it is observed in the soils but not in bedrock, and its abundance decreases with depth. The LOI values of the soils are higher than those observed in the DC1 samples, with a maximum in the topsoils (12–15%, Table 4A).

Clay characterization is consistent with the “chlorite” fraction consisting of chlorite, vermiculite and HIV in all soils from the planar transect (Appendix Tables 4 and 5). The mineral chlorite is absent from the topmost soils at SPRT and from one sample in the middle section of soil profile SPVF.

Major elements (except for Ca) show little variation with depth for the ridge top soils, but at the middle slope and valley floor sites, concentrations of major elements such as Al, Fe, Mg and K increase with depth while Si



Table 3

Cations in the CEC of Shale Hills parent and soils along the planar transect.

Sample depth (cm)	Soil pH	Al (mmol/kg)	Ca (mmol/kg)	K (mmol/kg)	Mg (mmol/kg)	Na (mmol/kg)	Si (mmol/kg)	Mn (mmol/kg)	CEC (+) (meq/kg)	Al/CEC <sup>a</sup> (%)
<i>Ridge top (SPRT)</i>										
0–10	3.99	7.22	5.60	2.04	1.61	0.17	0.08	2.66	43.9	49.3
10–20	4.10	6.09	5.71	1.91	1.66	0.32	0.07	1.66	38.9	47.0
20–30	3.84	8.00	2.70	1.48	0.93	0.16	0.09	0.53	34.3	69.9
<i>Middle slope (SPMS)</i>										
0–10	3.79	7.91	4.40	1.35	0.92	0.17	0.11	3.37	43.1	55.0
10–20	3.72	7.08	4.30	1.09	0.98	0.20	0.10	0.83	35.2	60.4
20–30	3.80	6.36	5.25	0.92	1.49	0.16	0.09	0.24	34.5	55.3
30–40	3.72	8.04	5.18	1.03	1.75	0.22	0.12	0.36	40.5	59.6
40–50	4.46	8.60	6.04	1.33	2.71	0.35	0.15	0.33	46.3	55.8
50–59	4.38	7.35	4.96	1.18	2.61	0.13	0.13	0.44	39.9	55.2
<i>Valley floor (SPVF)</i>										
0–10	4.42	5.22	11.98	1.34	9.68	0.22	0.08	1.60	64.1	24.4
10–20	4.44	2.70	11.04	1.47	9.49	0.19	0.10	0.54	52.3	15.5
20–30	4.84	1.08	13.44	1.90	10.88	0.19	0.13	0.48	55.4	5.8
30–40	4.81	0.74	16.06	2.28	12.25	0.31	0.17	0.41	62.9	3.5
40–50	4.40	0.48	18.37	2.19	13.38	0.28	0.17	0.39	68.9	2.1
50–60	4.72	0.21	19.12	2.22	14.18	0.31	0.21	0.26	71.1	0.9
60–67	4.97	0.15	19.20	2.23	14.07	0.36	0.22	0.18	70.8	0.6
<i>Parent Shale</i>										
DC1 17		0.17	22.36	1.84	16.03	1.58	0.26	0.13	82.0	0.6
DC1 22		0.23	22.72	1.92	18.93	0.65	0.38	0.41	88.9	0.8
DC1 26		0.01	16.56	1.76	19.79	0.73	0.25	0.05	76.4	0.1
DC1 29		0.04	14.04	1.20	22.32	0.26	0.21	0.06	75.2	0.1
DC1 32		0.00	10.27	1.45	17.70	3.52	0.00	0.03	61.0	0.0

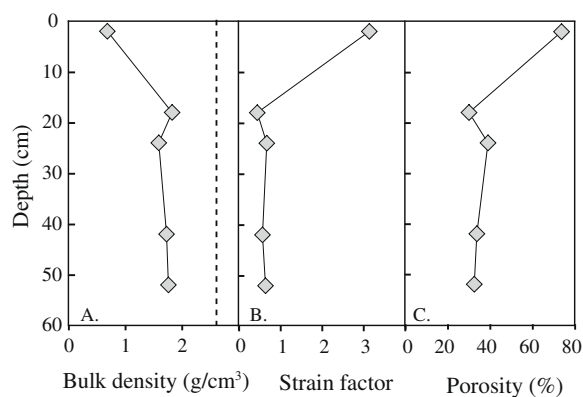
<sup>a</sup> Al/CEC ratio on an equivalent basis.

Fig. 3. (A) Bulk density measured at SPZR1 and SPZR2 cores along the planar transect. The soil grain density averages about 2.63 g/cm<sup>3</sup> (dashed line). (B) Strain factor calculated from bulk density for same cores. Positive values of strain indicate volume expansion during soil formation at SSHO. Ti instead of Zr was used as the immobile element for this calculation, which may overestimate the strain factor as discussed in text. (C) Total porosity calculated from bulk density and grain density. See text for details.

concentrations decrease (Table 4). The chemical composition of the duplicate cores (SPRT2, SPMS2, SPVF2, reported in Appendix Table 6) do not display significant variations from the primary core analyses. For the SPRT auger core, the rock fragment chips have higher Al, Fe,

Mg, K but lower Si, Zr, Ti concentrations than the corresponding bulk soils. Overall, the chemical composition of the chips is similar to that of the bedrock, except for Ca and Na.

Total Ca in SSHO soils and DC1 above 20 m is only about 0.1 wt.% and Ca concentrations are generally higher in surface soils. Relatively insignificant Mg and Ca concentrations were leached by 4 M acetic acid (<1 mmole/kg soil), consistent with little to no carbonate minerals (<0.01 wt.%) present in the soils.

### 3.3. Exchangeable cations

Cation concentrations in the exchangeable sites of five drill core samples and samples from three soil profiles along the 2D planar transect are presented in Table 3 and Fig. 4. The cation exchange capacity (CEC) of the parent shale ranges from 61 to 89 meq/kg dry soil with exchangeable sites dominantly occupied by Ca and Mg. The CEC of the three soil profiles, ranging from 34 to 71 meq/kg dry soil, increases downslope from the ridge top (SPRT), to middle slope (SPMS), to valley floor (SPVF) along the 2D planar transect (Fig. 4A–C). The deeper SPVF soils are similar to the parent shale with respect to capacity and composition of cation exchange sites, while the shallower soils have lower CEC. In the SPVF soils, the relative proportion of Al in the exchangeable sites is higher and the proportions of Mg and Ca decrease towards the surface (Table 3 and Fig. 4C). Cations in the exchangeable sites

Table 4A  
Elemental concentrations of Shale Hills soils, with corresponding Tau values, using Zr as an immobile element ( $\tau_{X_i}$ ).

Depth (cm)	Elemental concentrations												$\tau_{Zr,j}$ values										
	LOI (%)	Al (%)	Ca (%)	Fe (%)	K (%)	Mg (%)	Mn (%)	Na (%)	P (%)	Si (%)	Ti (%)	Zr (ppm)	Al	Ca	Fe	K	Mg	Mn	Na	P	Si	Ti	
SPRT																							
0-10	15.3	7.20	0.12	3.76	1.98	0.51	0.46	0.38	0.10	27.49	0.62	273	-0.56	-0.34	-0.56	-0.66	-0.65	2.81	-0.31	0.13	-0.33	-0.37	
10-20	11.3	7.36	0.17	4.00	2.13	0.56	0.36	0.39	0.13	28.98	0.64	275	-0.56	-0.08	-0.53	-0.63	-0.62	1.95	-0.29	0.53	-0.30	-0.35	
20-30	7.66	7.41	0.06	4.28	2.35	0.59	0.12	0.25	0.07	31.13	0.67	246	-0.50	-0.61	-0.44	-0.55	-0.55	0.15	-0.49	-0.14	-0.16	-0.25	
SPMS																							
0-10	12.6	6.51	0.15	2.98	1.74	0.43	0.31	0.49	0.12	29.96	0.71	351	-0.69	-0.37	-0.73	-0.77	-0.77	1.01	-0.31	0.12	-0.43	-0.43	
10-20	7.21	6.93	0.09	3.25	2.07	0.49	0.10	0.28	0.05	32.86	0.71	329	-0.65	-0.58	-0.68	-0.70	-0.72	-0.30	-0.57	-0.53	-0.33	-0.40	
20-30	6.65	7.20	0.11	3.60	2.22	0.55	0.05	0.48	0.08	32.07	0.65	295	-0.60	-0.43	-0.61	-0.64	-0.65	-0.58	-0.19	-0.14	-0.28	-0.38	
30-40	7.22	7.62	0.08	3.97	2.32	0.62	0.07	0.44	0.05	31.60	0.64	288	-0.56	-0.60	-0.55	-0.62	-0.60	-0.45	-0.24	-0.46	-0.27	-0.39	
40-50	7.77	8.10	0.10	4.26	2.57	0.66	0.06	0.47	0.08	31.46	0.64	277	-0.52	-0.47	-0.50	-0.56	-0.55	-0.49	-0.15	-0.09	-0.24	-0.36	
50-59	7.01	8.63	0.06	4.55	2.82	0.71	0.09	0.47	0.04	30.71	0.64	266	-0.46	-0.64	-0.45	-0.50	-0.50	-0.27	-0.12	-0.47	-0.23	-0.33	
SPVF																							
0-10	11.7	5.28	0.15	2.50	1.64	0.36	0.09	0.39	0.08	31.88	0.70	349	-0.75	-0.36	-0.77	-0.78	-0.80	-0.39	-0.44	-0.23	-0.39	-0.45	
10-20	7.51	6.88	0.11	3.31	2.24	0.52	0.07	0.35	0.03	31.83	0.68	318	-0.64	-0.50	-0.66	-0.67	-0.69	-0.50	-0.45	-0.65	-0.33	-0.41	
20-30	7.67	8.63	0.13	4.08	2.80	0.72	0.08	0.37	0.06	30.20	0.65	258	-0.45	-0.26	-0.49	-0.49	-0.47	-0.32	-0.28	-0.24	-0.22	-0.29	
30-40	7.56	9.05	0.11	4.45	3.05	0.78	0.07	0.35	0.04	28.33	0.62	219	-0.32	-0.23	-0.34	-0.34	-0.33	-0.27	-0.21	-0.36	-0.14	-0.21	
40-50	7.53	9.74	0.13	4.79	3.22	0.85	0.08	0.42	0.04	28.70	0.64	208	-0.22	-0.08	-0.25	-0.27	-0.23	-0.15	0.01	-0.39	-0.08	-0.15	
50-60	7.25	10.21	0.12	5.04	3.35	0.89	0.08	0.30	0.04	27.67	0.61	182	-0.07	-0.01	-0.10	-0.13	-0.08	-0.03	-0.19	-0.31	0.01	-0.07	
60-67	6.84	10.32	0.11	5.22	3.50	0.92	0.07	0.37	0.04	26.93	0.61	191	-0.11	-0.11	-0.12	-0.13	-0.09	-0.17	-0.03	-0.26	-0.06	-0.12	
Chips from SPRT																							
0-10	10.27	0.06	5.88	3.59	0.87			0.19	0.09	27.81	0.57	180	-0.06	-0.53	0.06	-0.06	-0.09		-0.49	0.56	0.03	-0.12	
10-20	11.75	0.05	5.04	4.37	0.99			0.22	0.06	26.79	0.61	150	0.30	-0.51	0.09	0.38	0.24		-0.26	0.22	0.19	0.13	
20-30	11.11	0.04	5.20	4.03	0.95			0.20	0.05	27.95	0.59	165	0.12	-0.62	0.02	0.15	0.08		-0.40	0.02	0.13	-0.01	

Table 4B

Elemental concentrations of Shale Hills soils, with corresponding Tau values, using Ti as an immobile element ( $\tau_{Ti,j}$ ).<sup>a</sup>

Depth (cm)	Elemental concentrations										$\tau_{Ti,j}$ values							
	Al (%)	Ca (%)	Fe (%)	K (%)	Mg (%)	Mn (%)	Na (%)	Si (%)	Ti (%)	Ti* (%)	Al	Ca	Fe	K	Mg	Mn	Na	Si
<i>WRT</i>																		
0–11	10.00	0.02	5.78	3.34	0.71	0.15	0.15	27.26	0.62	0.89	–0.33	–0.89	–0.25	–0.36	–0.46	0.37	–0.70	–0.27
11–15	9.47	0.03	5.25	3.05	0.65	0.14	0.15	27.38	0.64	0.98	–0.43	–0.86	–0.38	–0.47	–0.55	0.17	–0.73	–0.33
15–19	8.79	0.03	5.43	2.76	0.65	0.11	0.13	28.42	0.62	0.82	–0.36	–0.84	–0.23	–0.43	–0.46	0.14	–0.72	–0.17
19	10.85	0.01	5.56	3.88	0.80	0.04	0.16	27.30	0.62	0.62	0.04	–0.91	0.04	0.06	–0.14	–0.52	–0.54	0.05
<i>SPZR1</i>																		
6–0	2.37	0.52	1.06	0.36	0.13	0.40	0.09	7.33	0.15	0.25	–0.44	10.01	–0.51	–0.76	–0.64	12.21	–0.36	–0.30
12–22	7.57	BDL	3.95	2.08	0.49	0.07	0.12	29.17	0.61	0.76	–0.40	–1.00	–0.39	–0.53	–0.56	–0.25	–0.72	–0.08
<i>SPZR2</i>																		
0–3	5.88	BDL	2.93	1.44	0.31	0.25	0.15	26.51	0.56	1.02	–0.66	–1.00	–0.67	–0.76	–0.80	1.00	–0.74	–0.38
20–23	7.20	0.03	3.57	2.23	0.47	0.02	0.24	30.80	0.60	0.85	–0.50	–0.78	–0.51	–0.55	–0.63	–0.78	–0.50	–0.13
38–41	8.95	BDL	4.44	2.95	0.62	0.02	0.24	29.03	0.59	0.74	–0.28	–1.00	–0.30	–0.32	–0.44	–0.74	–0.41	–0.06
48–51	8.84	BDL	4.52	2.81	0.60	0.03	0.21	29.03	0.60	0.70	–0.25	–1.00	–0.25	–0.32	–0.42	–0.64	–0.47	–0.01
54–59	9.21	0.01	4.76	3.21	0.63	0.02	0.20	26.46	0.55	0.60	–0.08	–0.88	–0.07	–0.08	–0.28	–0.68	–0.40	0.06

BDL, below detection limit; 0.01% for Ca.

<sup>a</sup> Zr concentrations were not measured in these soils. Assuming similar proportions of Ti were lost at the same depth between WRT and SPRT, between SPZR1 and SPMS, and between SPZR2 and SPVF, we reconstructed Ti concentrations (Ti\*) and used these for  $\tau$  calculations.

of the SPRT and SPMS are mainly comprised of Al (about 60%), with moderate amounts of Ca and Mg. Contributions of Na, K and Si to overall CEC remain relatively constant as a function of depth and position as compared to parent shale (DC1).

Cation exchange sites account for about 20% of the total Ca in the soils at SPRT and SPMS, and nearly 50% in the SPVF soils and DC1 shale samples (Total Ca in SSHO soils and DC1 above 20 m is only about 0.1 wt.%). In contrast, Al and Mg on the CEC sites are negligible compared to their contents in the bulk soils.

### 3.4. Stream water chemistry

Concentrations of major elements varied seasonally in stream waters, ranging from 20 to 45  $\mu\text{M}$  for K, 12 to 60  $\mu\text{M}$  for Na, 60 to 600  $\mu\text{M}$  for Ca, 70 to 200  $\mu\text{M}$  for Mg, and 70 to 130  $\mu\text{M}$  for Si. In comparison, the dissolved Fe and Al concentrations are much lower (0.1 to 1  $\mu\text{M}$  for Fe, and 0.5 to 5  $\mu\text{M}$  for Al). The stream pH values range from 5 to 6.5. The average molar ratios of element concentrations over the two year period for Mg:Si:K:Fe:Al equal approximately 1.5:1:0.35:0.005:0.01.

### 3.5. Basin-scale erosion rate

The  $^{10}\text{Be}$  concentration of the sediment,  $3.33 \times 10^8$  atoms  $\text{g}^{-1}$ , was interpreted as a basin scale erosion rate of 39 tons  $\text{km}^{-2} \text{y}^{-1}$  (15 m/Myrs) assuming steady state, the site-specific rock density of 2.6  $\text{g cm}^{-3}$ , and an integrated  $^{10}\text{Be}$  delivery rate of  $1.3 \times 10^6$  atoms  $\text{g}^{-1} \text{y}^{-1}$  (Bierman et al., 2008; 2009). This site-specific erosion rate is indistinguishable from the average rate of denudation for the entire Appalachian Mountain range ( $17 \pm 9$  m/Myrs) calcu-

lated using over 250 in-situ measurements of  $^{10}\text{Be}$  in catchment sediments sampled over the entire Appalachian region (Bierman et al., 2007).

## 4. DISCUSSION

### 4.1. Bedrock transformation and weathering fronts

Major elements such as K, Mg, Fe, Al, and Si are relatively homogeneous within 25 m of the drill core samples (Table 1; Fig. 2A). However, Ca concentrations in the drill core samples are relatively low from the surface to 20 m depth, and then increase as high as 1.8% below that depth. DC1 samples also show less variability in chip density with depth below 20 m. This transition at 20 m may be related to either a lithologic shift between a carbonate-poor and a carbonate-rich unit in the Rose Hill Formation or may be indicative of the reaction front for dissolution of carbonate. Due to its reactivity,  $\text{Ca} \pm \text{Fe} \pm \text{Mg} \pm \text{Mn}$  carbonate (e.g., ankerite) is expected to be one of the first minerals to dissolve.

Brantley and White (2009) have argued that carbonate minerals can be profile-controlling minerals in that dissolution of these fast-dissolving phases often precedes weathering of other minerals and promotes deep influx of water into bedrock at the base of the weathering zone. For example, White et al. (1999) have documented that dissolution of calcite occurs at 10 m depth in granite in Panola, Georgia. According to those authors, calcite dissolution controls dissolution of plagioclase such that the plagioclase reaction front exactly parallels the calcite front but lies at shallower depths. Although we cannot rule out a lithological change as an alternate explanation, the simplest interpretation of the Ca profile in DC1 is therefore that loss of Ca above

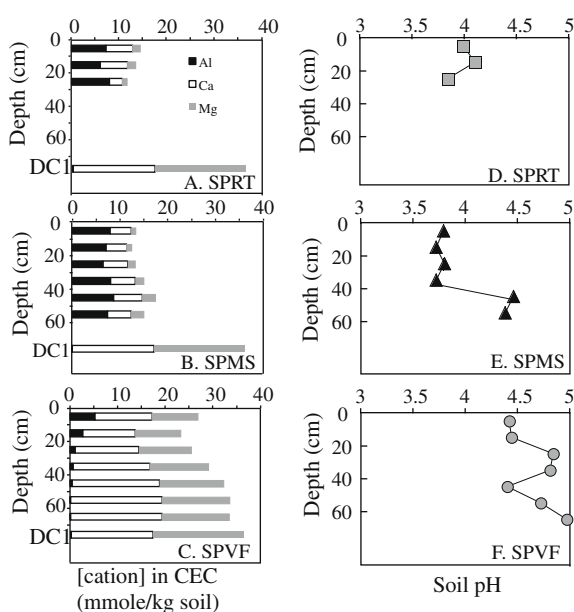


Fig. 4. Cation concentrations within the exchangeable sites at SPRT (A), SPMS (B) and SPVF (C) are plotted versus depth. Soil pH is plotted versus depth at SPRT (D), SPMS (E) and SPVF (F). The exchangeable cation concentrations averaged for DC1 site (bedrock) were plotted at the bottom of (A), (B) and (C) for comparison.

20 m depth represents dissolution of a carbonate mineral. If that is the case, the Ca profile in Fig. 2 thus represents the reaction front for ankerite in the system.

Likewise, the large variability in density above 6 m in the drilled shale chips may also be related to chemical factors. The similar chemistry observed between chips collected from SPRT and from drilled bedrock suggests that chips experience little chemical weathering with respect to K, Al, Fe, and Mg. Therefore, the loss of Ca and Na from the chips is attributed to feldspar dissolution that occurs before the clay mineral dissolution (Table 4). Most likely, the high Fe at 4.8 m and the change in chip size at about 17 m is related to the dissolution of feldspar and carbonate respectively and may correlate with the changes in density. Specifically, this uppermost zone demonstrates significant variability in Na and Ca chip concentrations, consistent with varying degrees of dissolution of feldspar.

The bottom-most soil bulk densities are similar to those measured in shallow drill core samples, consistent with our inference that DC1 samples can be considered as parent material. In the soils, clay minerals start to dissolve as described below and the bulk density decreases towards the ground surface (Fig. 3). Thus, the reaction fronts inferred at depth for carbonate (20 m) and feldspar (6 m) are overlain by weathering fronts for clay minerals. We have no evidence to suggest that these clay reactions extend into bedrock.

#### 4.2. Strain and element immobility

Our analysis of SSHO soils relies on the determination of elements that are mobilized from the soil and those that remain immobile. Elements that are commonly immobile in

soils include Zr, Ti, and Nb (Brimhall and Dietrich, 1987; Chadwick et al., 1990; Taylor and Blum, 1995; White et al., 1996; Price et al., 2005), although the mobility depends upon mineralogy and porewater composition (Kurtz et al., 2000; Neaman et al., 2006). In the soils at SSHO, Ti/Zr ratios decrease towards the land surface to values consistent with up to 45% loss of Ti. SiO<sub>2</sub> in quartz is also commonly used as a conservative component in sedimentary environments (White et al., 1996, 2008). At SSHO, quartz/Zr ratios are similar between bedrock shale and soils, consistent with little mobility of either quartz or Zr (Table 2). Thus, Zr, which we have only observed to be present as the relatively insoluble mineral zircon, is assumed to be the most immobile element in the analyzed soils.

The ratios of the volume of the soil ( $V_w$ ) to that of parent ( $V_p$ ) were assessed at SSHO by calculating the strain factor  $\varepsilon_{i,w}$  (Brimhall and Dietrich, 1987; Anderson et al., 2002):

$$\varepsilon_{i,w} = \frac{V_w}{V_p} - 1 = \frac{\rho_p}{\rho_w} \frac{C_{i,p}}{C_{i,w}} - 1 \quad (1)$$

Here,  $\rho$  refers to bulk density of parent (subscript  $p$ ) or weathered material ( $w$ ), and  $C$  refers to concentration of immobile or mobile elements ( $i, j$ , respectively). Positive  $\varepsilon$  values indicate expansion, a value of zero indicates iso-volumetric soil formation, and negative values indicate compaction. For example, deep regolith commonly develops iso-volumetrically on granite, i.e., soil thickness is equivalent to the initial thickness of parent material (White et al., 2005). Soils in karst regions, in contrast, collapse significantly due to preferential dissolution of carbonate minerals (Jin et al., 2008).

The calculated value of  $\varepsilon_{i,w}$  depends upon choice of immobile element. Given that we only measured bulk density of a few soil samples but did not measure Zr concentrations in those samples, to investigate strain we here only assess values of  $\varepsilon_{Ti,w}$ . Using 2.6 g/cm<sup>3</sup> as  $\rho_p$ , the calculated values of  $\varepsilon_{Ti,w}$  are positive for SPZR1 and SPZR2, ranging from 0.5 to 3.5, consistent with expansion of soils (Fig. 3B). These reported strain values based on Ti are presumed to be larger than  $\varepsilon_{Zr,w}$ , given the significant amount of Ti that has been lost. If we correct  $\varepsilon$  by assuming 45% loss of Ti, this yields strain values from 0 (no volume change) to 2 (doubling in soil volume). Therefore, soil expands during development.

Another calculation that can be made and which does not depend upon immobile elements is the calculation of total porosity  $\phi_t$  from bulk and grain density:

$$\phi_t = \left(1 - \frac{\rho_w}{\rho_g}\right) * 100\% \quad (2)$$

The porosity in the surface layer is as high as 70% and decreases with depth to 40% (Fig. 3C).

#### 4.3. Elemental changes along the planar transect

We use the assumption of immobility of Zr or Ti to also calculate relative loss or gain of elements. The behavior of elemental concentrations as a function of depth in regolith



and bedrock can be categorized with respect to simple end-member types (Brantley et al., 2007, 2008; Brantley and White, 2009). The end-member types relevant to SSHO are immobile profiles that show concentrations close to parent at all depths and depletion profiles wherein the elements are depleted at the surface but approach parent concentration at depth.

To assess the elemental profiles, it is necessary to first correct for the effects of expansion/compaction and for relative changes in concentrations due to changes in other elements in the soils. The value of  $\tau$ , the mass transfer coefficient, is therefore calculated according to the following equation (Brimhall and Dietrich, 1987; Anderson et al., 2002):

$$\tau_{i,j} = \frac{C_{j,w}}{C_{j,p}} \frac{C_{i,p}}{C_{i,w}} - 1 \quad (3)$$

Positive  $\tau_{i,j}$  values indicate enrichment of element  $j$ , negative values mean depletion and zero means element  $j$  is immobile in the weathered soils ( $w$ ) with respect to parent ( $p$ ). In fact,  $\tau_{i,j}$  equals the fraction of element  $j$  that was lost from the soil for  $\tau_{i,j} < 0$  and the relative enrichment factor for element  $j$  when  $\tau_{i,j} > 0$ . The  $\tau_{i,j}$  values computed for all profiles are reported in Table 4.

Fe, K, Mg, Si and Al show depletion profiles in the 1D site (WRT) and in all five soils along the planar 2D transect (Fig. 5). However, in contrast to SPVF, the deepest soils of the WRT, SPRT, SPZR1 and SPMS sites do not reach parent composition. The shallow soils at the upslope sites may have been homogenized by physical and biological mixing such as animal burrowing and tree throw. If mixing is the major reason for subvertical  $\tau_{i,j}$  plots (Fig. 5), then mixing processes are almost as fast as chemical weathering in the shallow ridgetop soils but are slower than such weathering in the thicker soils at SPMS and SPVF. However, bioturbation has been shown to be ineffective in mixing the soils in New England where snow cover can be significant (Kaste et al., 2007). Given the relatively similar climate between PA and New England, we argue that the subvertical  $\tau$  plots are not well explained simply by mixing. The chips recovered from the SPRT site are depleted with respect to Na, Ca but not other major elements such as K, Mg, Al and Fe, suggesting feldspar dissolution is prior to clay weathering (Fig. 5G).

Given our observations of leaching of elements such as Ca and Na in the bedrock, the best explanation for subvertical  $\tau$  plots is probably that unweathered bedrock has not been reached at the layer of augering refusal at the WRT, SPRT, SPZR1 and SPMS sites. As stated previously, these bottom-most samples lie within  $1\sigma$  of the mean for DC1; however, this relative error in estimation of parent composition is large enough to explain the discrepancy in Fig. 5. To exemplify this idea, we have drawn two horizontal lines on Fig. 5B, one to indicate the depth of refusal of augering (physical definition of bedrock) and one to indicate the inferred depth of chemically unaltered bedrock (chemical definition of bedrock). The latter was defined by visually extrapolating the  $\tau$  plots to  $\tau = 0$ .

Within each soil profile on the planar transect, the relative proportions of depletion are similar among Al, Fe, K,

and Mg. For example, the SPRT site has lost 55% of K and Mg, 50% of Al and about 44% of Fe. As Al, Fe, Mg and K occur in the chlorite and illite (see next section), similar fractional depletion for these two minerals, as discussed later. This conclusion is also consistent with similar grain densities observed for the soils and the parent shale.

Due to the presence of inert quartz, Si shows less depletion than K and Mg. Similarly, Na and Ca are depleted to a lesser extent than K and Mg (e.g., by about 30%) at all three sites, presumably due to feldspar dissolution (Table 4). Values of  $\tau_{Mg}$ , contoured based on the five soil profiles along the planar transect using Origin software (Fig. 5H), document that the extent of Mg depletion is higher in the upper hillslope, decreasing towards the valley floor.

#### 4.4. Mineral transformations

Soil mineralogy was compared to the parent shale to understand weathering reactions as a function of depth and landscape location (e.g., White et al., 1996; Murphy et al., 1998; White et al., 2001; Burke et al., 2007; Brantley and White, 2009). Depletions or enrichments of the dominant minerals illite and “chlorite” ( $j$ ) were evaluated by calculating  $\tau_{Zr,j}$  from Eq. (2), using mineral abundances instead of elemental concentrations. Uncertainty in mineral  $\tau_{Zr,j}$  was evaluated in the same fashion as for elemental  $\tau_{Zr,j}$  values by assuming that relative error in mineral quantification is 5%. Both “chlorite” and illite showed depletion profiles, indicating significant loss of “chlorite” and illite especially from the shallow soils (Fig. 6A–C). This observation is consistent with the significant depletion of K, Mg, Al, Si, and Fe in soils (Fig. 5). Quartz remains relatively immobile (Fig. 6A–C).

Previous studies in a variety of climates and soil types have demonstrated that chlorite and illite weathering generally occurs through a series of clay transformation reactions (e.g., Klute, 1986; Bain et al., 1993; Lee et al., 2003; Wilson, 2004; Hseu et al., 2007). For example, Lee et al. (2003) showed that chlorite transformed into interstratified vermiculite–chlorite and vermiculite with progressive release of Mg and Fe from the brucite-layer of the chlorite structure in serpentinitic soils of northern California. Detailed clay characterization at SSHO showed vermiculite and HIV in all soils of the planar transect. Both phases share XRD peaks with chlorite (Appendix Tables 4 and 5), making it difficult to distinguish primary mineral phases from weathering products. However, because the charge and identity of the interlayer cations in chlorite, vermiculite, and HIV are different, we used the CEC of the soil and parent shale samples to characterize the clay transformations as described in the next section.

The shale bedrock (DC1) and soils at the valley floor (SPVF) have similar cation exchange capacity and composition, with  $Mg^{2+}$  and  $Ca^{2+}$  dominating exchange sites (Fig. 4C). The occurrence of vermiculite in the soils of the valley floor, especially the deepest soils, is consistent with the interpretation that the chlorite in the parent Rose Hill shale has a vermiculite component, i.e., “vermiculitized” chlorite. At SPVF,  $Al^{3+}$  concentrations in the cation ex-

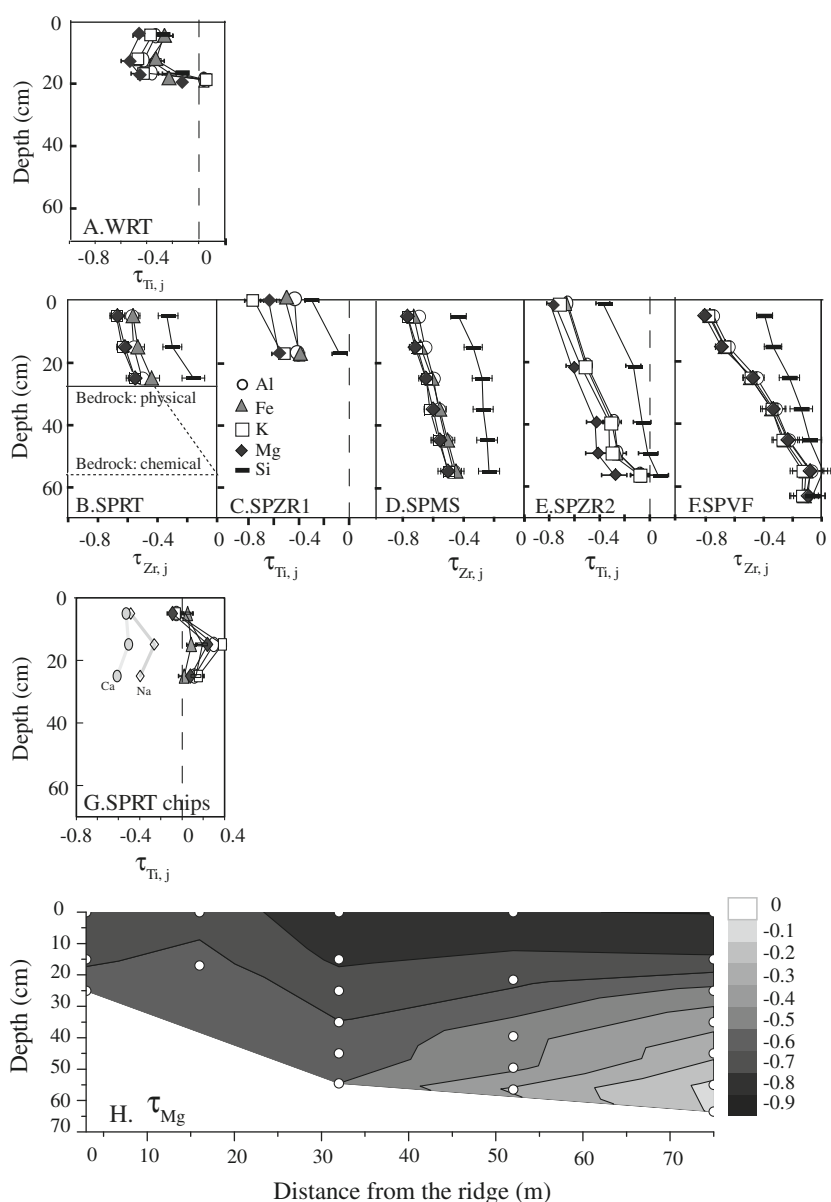


Fig. 5. Depletion of major elements in the 1D site sampled at the highest point in the catchment (A.WRT) and in five soil profiles along the 2D planar transect (B – SPRT at ridge top; C – SPZR1; D – SPMS at middle slope; E – SPZR2; F – SPVF at valley floor). Error bars indicate uncertainties in  $\tau$  calculation. Ti was used as the immobile element for (A), (C) and (E) (see Table 4 for details). In Figure 5B, one horizontal line indicates the depth of refusal of augering (physical definition of bedrock) and one indicates the inferred depth of chemically unaltered bedrock (chemical definition of bedrock). The latter was defined by visually extrapolating the  $\tau$  plots to  $\tau = 0$ . A contour map was made for  $\tau_{Mg}$  based on the 5 soil profiles along the 2D transect (H).

change sites increase upward in the soil profile while  $Mg^{2+}$  and  $Ca^{2+}$  concentrations decrease. In contrast, the CEC and its composition at SPRT and SPMS vary little with depth but differ significantly with DC1 samples, consistent with the previous conclusion that the soils at these two sites have not been sampled to the parent shale.

Importantly,  $Al^{3+}$  content in CEC becomes significant as weathering progresses, occupying up to 60% of the exchange sites at SPRT and SPMS. This is consistent with the observation that the soil pH showed an increase of pH with depth (Fig. 4D and E). A value of Al/CEC ratio of 60% (Table 3) as observed at SPRT and SPMS has been

described as the threshold value where Al starts to play a greater role in buffering acidity (Chadwick and Chorover, 2001). The high Al composition of the CEC also reflects the inferred hydrolysis and polymerization of Al in interlayers of vermiculite in acid soils such as those at SSHO (Graham et al., 1989).

Vermiculite formation generally reflects a structural inheritance from illite and chlorite. In contrast, when precipitation of kaolinite occurs during such clay transformations, it forms after the complete destruction of the 2:1 clay structure. Kaolinite, not detected in the parent bedrock, is present in concentrations up to 2.8 wt.% in the soils,

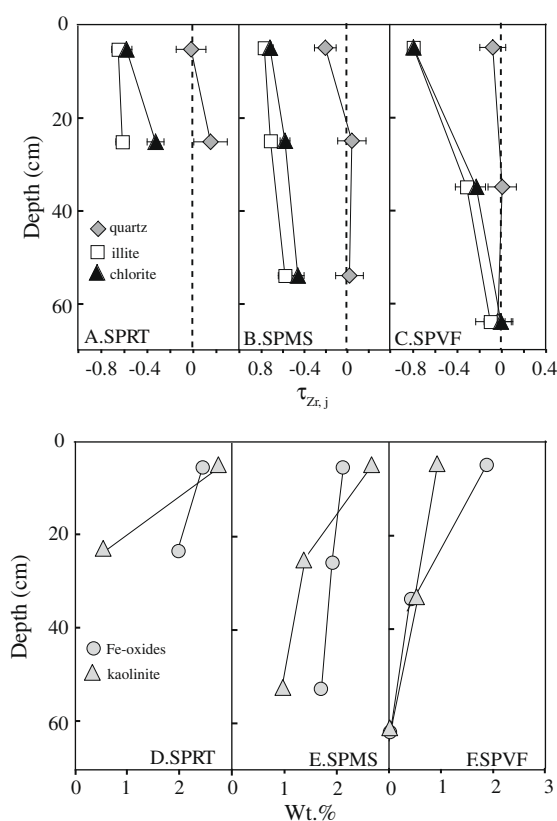


Fig. 6. Variation of primary mineral abundances relative to parent (dashed lines) at ridge top (A), middle slope (B), and valley floor (C); absolute abundances of kaolinite and Fe-oxides at ridge top (D), middle slope (E), and valley floor (F) along the planar transect. “Chlorite” and illite show depletion while quartz remains relatively unchanged versus depth. The fraction attributed to “chlorite” is assumed to be composed of chlorite, vermiculite and HIV, as described in the text.

increasing in abundance upward to the surface (Table 2; Fig. 6D, E, F). All of these characteristics are consistent with its presence as a weathering product. Kaolinite may also form due to feldspar dissolution, as negative values of  $\tau_{Na}$  are observed in all soils (Table 4). Kaolinite is known to be a stable secondary phase in temperate regions such as SSHO (Klute, 1986; Berner and Berner, 1996; Jin et al., 2008). The absence of smectite at Shale Hills is consistent with the fact that the catchment is well-drained and experiences a temperate climate (Helgeson et al., 1969; Berner and Berner, 1996; Price et al., 2005).

The sequence of mineral transformations in the soils developed on Rose Hill shale can be summarized in the following five reactions:

- (i) feldspars  $\rightarrow$  kaolinite
- (ii) illite  $\rightarrow$  vermiculite
- (iii) chlorite  $\rightarrow$  vermiculite
- (iv) vermiculite  $\rightarrow$  hydroxy interlayered vermiculite (HIV)
- (v) hydroxy interlayered vermiculite  $\rightarrow$  kaolinite + Fe-oxyhydroxide.

The similarity of K and Mg depletion profiles is suggestive of congruent dissolution of illite and chlorite (Fig. 5). However, dissolved Al and Fe concentrations in filtered stream waters averaged over 24 months at Shale Hills are less than  $5 \mu\text{M}$  and  $1 \mu\text{M}$ , respectively, not high enough to account for stoichiometric release of these elements from chlorite and illite dissolution. Thus, Fe and Al are not significantly lost from the SSHO soils as solutes that pass a  $0.45 \mu\text{m}$  filter. Instead, micron-sized Al- and Fe-rich particles are inferred to be lost from the soils. Since no accumulation of Al and Fe was observed at the soil–bedrock interface, these particles must be translocated downslope by flowing water.

Consistent with the inference of translocation, previous field studies and soil column experiments in France, Denmark, and Virginia have revealed that particles can be mobilized vertically in soil profiles by shear stresses in macropores at rates of about  $10\text{--}100 \text{ mg particle/L}$  (Laegdsmand et al., 1999; El-Farhan et al., 2000; Rousseau et al., 2004). The mobilized particles are generally several microns in size and consist of clay minerals (kaolinite), organic matter, and Fe-oxide/hydroxides (Kaplan et al., 1997). Particle transport is favored by high infiltration rate, high soil moisture content, and the presence of continuous macropores in the soil structures (Rousseau et al., 2004), all of which have been observed through soil moisture studies at SSHO (Lin, 2006).

Given that shales are characterized initially by fine grain size, particle translocation should be an important player once chemical dissolution has disaggregated the bedrock. Thus, we conclude that mobilization of Al- and Fe-bearing particles, especially secondary phases such as kaolinite and Fe-oxyhydroxide, is a very significant contributor to elemental mobility at SSHO. Given that Fe and Al accumulation was observed in SPVF, we also conclude that this particle transport occurs down the hillslope through the soil.

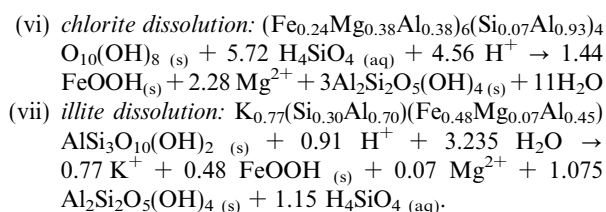
#### 4.5. Stoichiometric reactions

It is impossible to physically separate or quantitatively partition the two dominant minerals in the SSHO, “chlorite” and illite, because their physical and chemical properties are similar. In this section, a normative model of mass balance is therefore developed that is consistent with all observations – and especially the quantitative XRD information. The model is constructed to partition major elements into identified mineral phases. Samples used to constrain this exercise are soils from the planar transects and DC1 samples where carbonate minerals are known to be absent (above 20 m).

First, all of the measured Na and Ca concentrations were allocated to albite and anorthite, respectively. The K was then allocated to potassium feldspar until the total wt.% feldspar (albite + anorthite + K feldspar) equaled the feldspar fraction estimated from quantitative XRD (Table 2). Si was also allocated in the requisite amounts to feldspar. Next, the remaining Si was allocated to quartz until the wt.% of that phase equaled that measured by XRD. When kaolinite was observed using quantitative XRD, the appropriate amount of Al and Si was allocated to

kaolinite. Some Fe was allocated to Fe-oxide assuming a stoichiometry of FeOOH. Last, the remaining major cations (as K, Mg, Fe, Al, and Si oxides) were allocated to illite and chlorite to achieve the fraction observed for each clay with XRD. For this calculation, Fe was assumed to be Fe(III) in the illite and chlorite structure because the Rose Hill Formation is relatively oxidized, as evidenced by the presence of hematite and magnetite (Folk, 1960). A multiple-dimension linear regression was applied using a standard mineral composition (Kudrat et al., 2000) for “chlorite”,  $(\text{Fe}_a\text{Mg}_b\text{Al}_{1-a-b})_6(\text{Si}_{1.5b-0.5}\text{Al}_{1.5-1.5b})_4\text{O}_{10}(\text{OH})_8$ , and illite,  $\text{K}_{1+y-z}(\text{Si}_z\text{Al}_{1-z})(\text{Fe}_x\text{Mg}_y\text{Al}_{1-x-y})\text{AlSi}_3\text{O}_{10}(\text{OH})_2$ . The following stoichiometric coefficients were determined as best fits:  $a = 0.24$ ,  $b = 0.38$ ,  $c = 0.07$ ;  $x = 0.48$ ,  $y = 0.07$ ,  $z = 0.30$ .

Importantly, the “chlorite” phase discussed here is a model mineral that includes contributions from vermiculite and HIV. For this reason, Al is calculated to be present in greater abundance than in a typical chlorite (Kudrat et al., 2000). Using this mineral formula, the following stoichiometric weathering reactions were written as composite reactions describing reaction (i) through (iv) above:



In summary, dissolution of illite and chlorite forms more stable kaolinite through intermediate phases, followed by translocation of Fe-oxides and kaolinite as particles. Overall, Al and Fe are lost mostly as secondary phase particulates while  $\text{Mg}^{2+}$  and  $\text{K}^+$  were lost as solutes into the stream. Based on average streamwater chemistry and reactions (vi), and (vii), chlorite dissolution contributes 98% of the dissolved Mg; illite dissolution contributes 2% of dissolved Mg and almost 100% of dissolved K. Loss of Na and Ca also occurs as feldspar dissolution as shown in reaction (iv) above.

#### 4.6. Hillslope evolution along a planar transect

Soil development and the overall hillslope evolution are controlled by the soil production rate at the bedrock–soil interface ( $P$ ,  $\text{g m}^{-2} \text{ y}^{-1}$ ), and the total denudation rate ( $D$ ,  $\text{g m}^{-2} \text{ y}^{-1}$ ) (e.g., Fernandes and Dietrich, 1997; Anderson et al., 2002; Heimsath et al., 2005; Green et al., 2006; Yoo et al., 2007; Anderson et al., 2007). The denudation rate includes three components, the loss of mass as solutes, the loss of mass as fine particles throughout the soil profile, and the loss of bulk mineral particles due to erosion at the land surface. In the model we develop below, we define only two components, namely the “chemical” weathering rate  $W$  ( $\text{g m}^{-2} \text{ y}^{-1}$ ) and physical erosion rate  $E$  (in  $\text{g m}^{-2} \text{ y}^{-1}$ ). According to our definitions below, physical erosion removes weathered soil grains that have element ratios *identical* to bulk soil while “chemical” weathering as we define it

below removes some elements more rapidly than others. However, this latter transport includes both losses as solutes and fine particles.

To develop the model for the 2D transect, we make assumptions about erosion and soil production rates with respect to time. The margin of the last glacial advance lies approximately 60 km north of Shale Hills (Sevon and Braun, 1997). Periglacial features and deposits are observed in the SSHO and in central Pennsylvania (Ciolkosz et al., 1990; Gardner et al., 1991). The glacial advance boundary divides less well-developed soils to the north in Pennsylvania from thick, well-developed soils to the south (Ciolkosz et al., 1990). Periglacial activity has been hypothesized to be more effective in shaping the Appalachian landscape around the SSHO than temperate fluvial processes (Braun, 1989).

For example, studies in central Pennsylvania have shown that soils developed on slopes, especially south-facing slopes, have experienced downslope transport driven by intensive freezing and thawing (Carter and Ciolkosz, 1986). In some settings, unconsolidated fragments form a stratification of rhythmically layered deposits, interpreted as Grezes Litees (Clark and Ciolkosz, 1988). Grezes Litees on hillslope and riverine terraces have been identified to occur throughout Pennsylvania in the periglacial region (Clark and Ciolkosz, 1988), including the area occupied by the SSHO. However, such mixing and inverting of soils due to periglacial activity probably does not describe the ridgetop sites such as WRT or SPRT where little movement from upslope is likely. Furthermore, the chemistry-depth curves for the SPMS and SPVF sites (Fig. 5) document no evidence for mixing other than downslope creep. Thus, such a “mixed soils” scenario is not considered further here for the 1D or north-facing 2D transect.

Two other hypotheses are introduced here as end-member scenarios for geomorphological development of the north-facing planar transect at SSHO. In the “steady state” scenario, the hillslope, hypothesized to have been perturbed by the last glacial advance, has achieved a new steady state. With this hypothesis, the rate of bedrock to soil transformation equals the rate of chemical and physical erosion so that soils now maintain a time-independent thickness and chemistry (e.g., Roering et al., 2001). Under this scenario, the soil residence time at SSHO is estimated to  $\approx 20,000$  years by dividing the soil thickness at the ridge top (30 cm), by the denudation rate (15 m/Myrs from  $^{10}\text{Be}$  analysis). As expected, this residence time is much shorter than the time since deposition of the Rose Hill Formation (i.e., in the Silurian).

In the second “transient” scenario, soils may have been stripped or otherwise significantly perturbed during the most recent peri-glacial period, leaving behind exposed bedrock or very thin soils that began weathering 13,000 years ago in the warming climate. This scenario is consistent with the relatively high erosion rates of 150–300 m/Myrs that have been determined near the ancient ice margin in Pennsylvania: such a rate could have thinned soils significantly 13,000 years ago (Braun, 1989). In this scenario, the soils remain today in a transient condition and have not reached a new steady state thickness. As discussed below, we cannot



refute the transient hypothesis but we show that the system can be modeled as if it is in steady state without any significant contradictions.

We therefore first assume that soils are at steady state and test a mass-balance model for the three planar transect sites, following Yoo et al. (2007). In this treatment, the soil profile at the ridge top (SPRT site) is modeled as a 1D system, where water flows downward and soil material is lost both through chemical weathering and physical erosion. Input of sediment to the SPRT site is assumed negligible, given that the slope of the southern east-west ridgeline near SPRT is less than 5%. In contrast, at other locations along the planar transect (e.g., the middle slope SPMS site and valley floor SPVF site) water flowpaths are largely 2D, downward and along the slope. Although we cannot dismiss the possibility entirely, contributions from down-channel transport of sediments or solutes to the soils at SPVF are thought to be minimal given the relatively high position of this site. As shown below, no contradictions are encountered with this assumption.

Instead of using chemistry fitting-iteration methods used by previous researchers (Yoo et al. 2007), we assume that sediment transport occurs in steps between three boxes (e.g., SPRT → SPMS → SPVF; Fig. 1B). The sediment erosion and weathering rates are assumed to be the same within each box. Given that the distance between SPRT and SPVF is roughly 75 m, we thus set the length of each box to be 25 m (denoted as  $L$ ).

Biota can significantly take up nutrients such as K, thereby affecting their loss from a system as solutes (e.g., Taylor and Velbel 1991; Amundson et al., 2007). However, given the long time-scale (thousands of years) of soil formation at SSHO, we can assume that biota exists at steady state, i.e., uptake of nutrients into biota are balanced by outputs from biota as fresh litter. In the model, biota therefore do not represent net sources or sinks.

If the thickness of soils along the hillslope is at steady state, then the total denudation rate  $D$  equals the soil production rate  $P$  for the transect:

$$P = D = W + E \quad (4)$$

The average soil chemistry for each site (SPRT, SPMS, SPVF) was calculated by averaging the compositions for each sampled soil interval weighted by soil density and thickness ( $C_{j,SPRT}$ ,  $C_{j,SPMS}$ ,  $C_{j,SPVF}$ , as summarized in

Table 5A). At the ridge top, no sediment from above was assumed to be added to the soil, so mass balance equations can be written for immobile ( $i$ ) (5) and mobile elements ( $j$ ) (6):

$$P^{SPRT} C_{i,p} = E^{SPRT} C_{i,SPRT} \quad (5)$$

$$P^{SPRT} C_{j,p} = E^{SPRT} C_{j,SPRT} + W_j^{SPRT} \quad (6)$$

Rearranging Eqs. (4)–(6), the total chemical weathering rates,  $W$ , and weathering rates of each element,  $W_j$  (in  $\text{g m}^{-2} \text{y}^{-1}$ ), are calculated based on average soil chemistry at the ridge top:

$$W^{SPRT} = P^{SPRT} \left( 1 - \frac{C_{i,p}}{C_{i,SPRT}} \right) \quad (7)$$

$$W_j^{SPRT} = P^{SPRT} \left( C_{j,p} - \frac{C_{i,p}}{C_{i,SPRT}} C_{j,SPRT} \right) = -P^{SPRT} C_{j,p} \tau_{j,SPRT} \quad (8)$$

As seen from Eq. (9),  $W_j$  is a function of the depletion factor  $\tau_j$ . The sum of  $W_j$  for all elements equals  $W$  for each site. The fraction of chemical weathering relative to the total denudation flux is defined as the chemical depletion factor (CDF) (Riebe et al., 2003):

$$\text{CDF}^{SPRT} \equiv \frac{W^{SPRT}}{P^{SPRT}} = \frac{W^{SPRT}}{D^{SPRT}} = 1 - \frac{C_{i,p}}{C_{i,SPRT}} \quad (9)$$

The CDF can also be defined on an elemental basis, i.e.,  $\text{CDF}_j$  is the fraction of loss of element  $j$  due to chemical weathering to overall production rate of  $j$  and is related to  $\tau$  (Table 4):

$$\text{CDF}_j^{SPRT} = -\tau_{j,SPRT} \quad (10)$$

The physical erosion  $E^{SPRT}$  ( $\text{g m}^{-2} \text{y}^{-1}$ ) and sediment flux out of the ridge top site,  $Q^{SPRT}$  ( $\text{g m}^{-1} \text{y}^{-1}$ ), can be calculated as:

$$E^{SPRT} = P^{SPRT} \frac{C_{i,p}}{C_{i,SPRT}} \quad (11)$$

$$Q^{SPRT} = E^{SPRT} L \quad (12)$$

Here  $L$  is the length of the box, i.e., 25 m.

For the middle slope site, net physical erosion is defined as the gradient of the sediment flux:

Table 5A  
Averaged soil chemistry at each site along the hillslope.

	Ridge top SPRT	SPZR1	Middle slope SPMS	SPZR1	Valley floor SPVF
Al (%)	7.35	7.36	7.59	8.34	8.85
Ca (%)	0.12	0.02	0.09	0.01	0.12
Fe (%)	4.08	3.83	3.85	4.21	4.33
K (%)	2.19	2.01	2.34	2.69	2.92
Mg (%)	0.56	0.48	0.59	0.56	0.75
Na (%)	0.33	0.12	0.43	0.22	0.36
Si (%)	29.63	28.27	31.63	28.57	29.19
Zr (ppm)	263		296		238
Fe/Al (molar)	0.27		0.24		0.24
K/Al (molar)	0.21		0.21		0.23
Mg/Al (molar)	0.09		0.09		0.10
Si/Al (molar)	3.89		4.02		3.18

$$E^{\text{SPMS}} = (Q^{\text{SPMS}} - Q^{\text{SPRT}})/L \quad (13)$$

$$P^{\text{SPMS}} = E^{\text{SPMS}} + W^{\text{SPMS}} \quad (14)$$

This can be written for immobile (*i*) and mobile elements (*j*):

$$P^{\text{SPMS}} C_{i,p} = (Q^{\text{SPMS}} C_{i,\text{SPMS}} - Q^{\text{SPRT}} C_{i,\text{SPRT}})/L \quad (15)$$

$$P^{\text{SPMS}} C_{j,p} = (Q^{\text{SPMS}} C_{j,\text{SPMS}} - Q^{\text{SPRT}} C_{j,\text{SPRT}})/L + W_j^{\text{SPMS}} \quad (16)$$

By rearranging Eqs. (14)–(17), we derive:

$$W^{\text{SPMS}} = P^{\text{SPMS}} \left(1 - \frac{C_{i,p}}{C_{i,\text{SPMS}}}\right) + E^{\text{SPRT}} \left(1 - \frac{C_{i,\text{SPRT}}}{C_{i,\text{SPMS}}}\right) \quad (17)$$

$$E^{\text{SPMS}} = P^{\text{SPMS}} \frac{C_{i,p}}{C_{i,\text{SPMS}}} - E^{\text{SPRT}} \left(1 - \frac{C_{i,\text{SPRT}}}{C_{i,\text{SPMS}}}\right) \quad (18)$$

$$Q^{\text{SPMS}} = \left(P^{\text{SPMS}} \frac{C_{i,p}}{C_{i,\text{SPMS}}} + E^{\text{SPRT}} \frac{C_{i,\text{SPRT}}}{C_{i,\text{SPMS}}}\right)L \quad (19)$$

$$W_j^{\text{SPMS}} = P^{\text{SPMS}} C_{j,p} \left(1 - \frac{C_{j,\text{SPMS}} C_{i,p}}{C_{j,p} C_{i,\text{SPMS}}}\right) + E^{\text{SPRT}} C_{j,\text{SPRT}} \left(1 - \frac{C_{j,\text{SPMS}} C_{i,\text{SPRT}}}{C_{j,\text{SPRT}} C_{i,\text{SPMS}}}\right) \quad (20)$$

$$\text{CDF}^{\text{SPMS}} = \frac{W^{\text{SPMS}}}{P^{\text{SPMS}}} = 1 - \frac{C_{i,p}}{C_{i,\text{SPMS}}} + \frac{E^{\text{SPRT}}}{P^{\text{SPMS}}} \left(1 - \frac{C_{i,\text{SPRT}}}{C_{i,\text{SPMS}}}\right) \quad (21)$$

The same equations can be written for the SPVF site, with sediment transport from the SPMS site defining input to the valley floor site. For both the SPMS and SPVF sites, we have assumed only downslope nonconvergent transport

of sediments and solutes along the hillslope. However, for the SPVF site we further assume no input of sediments or solutes except from the 2D transect (i.e., the site is high enough above the alluvial channel that no inputs were derived from the channel). In using this formulation of the model, the value of  $W_j$  is the net loss or gain of element *j* attributed to weathering processes from each site along the hillslope. The weathering flux,  $F_j$  ( $\text{g m}^{-1} \text{y}^{-1}$ ) out of each box can be calculated by integrating weathering rates calculated with Eq. (9) or Eq. (21) over distance:

$$F_j^{\text{SPRT}} = W_j^{\text{SPRT}} L \quad (22)$$

$$F_j^{\text{SPMS}} = W_j^{\text{SPMS}} L + F_j^{\text{SPRT}} \quad (23)$$

$$F_j^{\text{SPVF}} = W_j^{\text{SPVF}} L + F_j^{\text{SPMS}} \quad (24)$$

The denudation rate of 15 m/Myrs was measured at SSHO by meteoric  $^{10}\text{Be}$ . The soil production rate (*P*) can be set equal to 15 m/Myrs for the whole transect assuming this is a steady-state system. Thus, with soil chemistry and soil production rate known for each site, erosion (*E*), weathering rates (both *W* and  $W_j$ ), sediment fluxes (*Q*) and weathering fluxes ( $F_j$ ) are calculated (Table 5B). Importantly, 30–50% (CDF) of the total elemental loss is due to chemical dissolution from the ridge top and the middle slope sites (Fig. 7A). Of this total major elemental loss at these two sites, Si and Al together account for almost 70% of chemical weathering loss, followed by Fe (13%), K (7%) and Mg oxides (3%).

In contrast to the soils at ridge and midslope, chemical processes led to both accumulation and outfluxes at the valley floor site, SPVF. The outfluxes of Al, K, Fe and Mg from the SPVF can be considered as the chemical contribution of the planar transect as a whole to the catchment:

Table 5B  
Mass-balance model results.

	<i>P</i> = 15 m/Myrs			<i>P</i> decays <sup>a</sup>		
	Ridge top	Middle slope	Valley floor	Ridge top	Middle slope	Valley floor
<i>P</i> ( $\text{g m}^{-2} \text{yr}^{-1}$ )	37.2	37.2	37.2	37.2	19.7	16.5
<i>W</i> ( $\text{g m}^{-2} \text{yr}^{-1}$ )	12.0	17.7	−1.5	12.0	10.7	−4.2
<i>E</i> ( $\text{g m}^{-2} \text{yr}^{-1}$ )	25.2	19.5	38.7	25.2	9.0	20.7
CDF <sup>b</sup>	0.3	0.5	0.0	0.3	0.5	−0.3
<i>F</i> ( $\text{g m}^{-1} \text{yr}^{-1}$ )	300	742	704	300	567	463
<i>Q</i> ( $\text{g m}^{-1} \text{yr}^{-1}$ )	630	1118	2086	630	854	1371
$F_{\text{Al}}^c$ ( $\text{g m}^{-1} \text{yr}^{-1}$ )	54	115	115	54	88	76
$F_{\text{Ca}}$ ( $\text{g m}^{-1} \text{yr}^{-1}$ )	0.4	1.2	0.8	0.4	0.9	0.5
$F_{\text{Fe}}$ ( $\text{g m}^{-1} \text{yr}^{-1}$ )	26	59	63	26	45	42
$F_{\text{K}}$ ( $\text{g m}^{-1} \text{yr}^{-1}$ )	21	44	44	21	33	29
$F_{\text{Mg}}$ ( $\text{g m}^{-1} \text{yr}^{-1}$ )	5	11	11	5	8	7
$F_{\text{Na}}$ ( $\text{g m}^{-1} \text{yr}^{-1}$ )	1.2	1.8	2.5	1.2	1.4	1.6
$F_{\text{Si}}$ ( $\text{g m}^{-1} \text{yr}^{-1}$ )	62	143	136	62	109	89
Fe/Al <sup>d</sup> (molar)	0.23	0.25	0.26	0.23	0.25	0.26
K/Al (molar)	0.27	0.26	0.26	0.27	0.26	0.26
Mg/Al (molar)	0.11	0.11	0.10	0.11	0.11	0.10
Si/Al (molar)	1.1	1.2	1.1	1.1	1.2	1.1

<sup>a</sup> *P* = 15 m/Myrs at the ridge top, and decays exponentially with soil thickness along the transect.

<sup>b</sup> CDF (chemical depletion factor) = *W*/*P* (see text for details).

<sup>c</sup>  $F_j$  is the outflux of element *j*; thus,  $F_{j,\text{SPMS}} = F_{j,\text{SPRT}} + W_{\text{SPMS}} L$ ,  $F_{j,\text{SPVF}} = F_{j,\text{SPMS}} + W_{\text{SPVF}} L$ , and  $F_{\text{SPRT}} = W_{\text{SPRT}} L$ , where *L* is 25 m, the length of the box along the hillslope.

<sup>d</sup> Molar ratio of chemical weathering fluxes  $F_j$ , very similar to those in the soils except for Si.

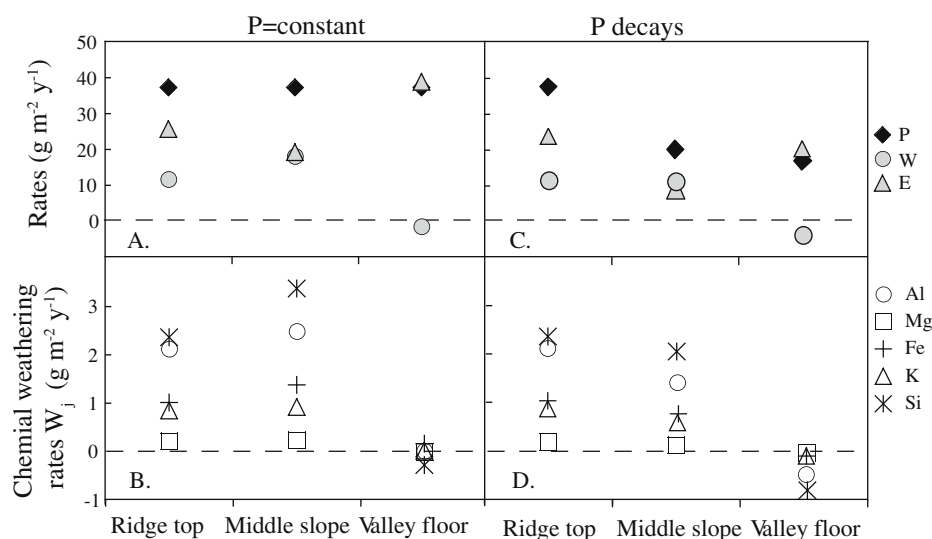


Fig. 7. Model results for relative contributions of net chemical weathering fluxes ( $W$ ) and net physical erosion fluxes ( $E$ ) to the overall soil production rate assuming the latter is constant (A;  $P = 15 \text{ m/Myrs} = 37.2 \text{ g m}^{-2} \text{ y}^{-1}$ ) or is variable (C;  $P = 37.2 \text{ g m}^{-2} \text{ y}^{-1}$  at ridge top but decreases exponentially with increasing soil thickness). Notice the negative chemical weathering rates, or accumulation instead of loss, in valley floor. Chemical weathering rates of individual elements ( $W_j$ ) as a function of topographic position are also plotted for the two modeling scenarios (B, D).

importantly, the chemical losses are proportional among these elements, with relative ratios similar to stoichiometry of average soil chemistry (Table 5B). In contrast, the ratio of  $F_{Si}$  to  $F_j$  for  $j = \text{K, Mg, Fe, Na}$  does not match the stoichiometric ratios in the shale, presumably because Si mainly occurs as the unreactive mineral quartz in the shale. As discussed previously, the molar ratios of the gradients in Al, K, Fe and Mg versus depth in the SPVF profile are equal to the ratios of those elements in illite and chlorite. These two lines of evidence are consistent with congruent dissolution of illite and chlorite according to reactions (vi) and (vii).

As formalized in the equations above, this mass balance calculation depends greatly on the accurate determination of Zr concentrations in the parent and weathered materials. Furthermore, erosion ( $E$ ) is considered to be loss of soil particles, i.e., particles that contain Zr, while chemical weathering ( $W$ ) is considered to be loss of mass that is chemically distinct from the average soil – this latter is either loss of solutes or loss of particles that do not contain Zr. In effect, we rely upon the observation from SEM analysis that Zr is present as zircons in the shale, and we assume that zircons with density of  $4.6 \text{ g/cm}^3$  are not lost as subsurface particle transport of kaolinite and Fe-oxyhydroxide particles throughout the profiles. These largely Zr-free particle fluxes are described by the  $W$  and  $W_j$  terms rather than by  $E$  in our model. For this reason,  $W$  is referred to as the nonstoichiometric or the “chemical” weathering term.

As mentioned previously, relatively high concentrations of K, Si and Mg are measured in stream water; thus, transport of these elements is attributed primarily to soluble loads. In contrast, stream water Al and Fe concentrations are so low that transport of these elements is attributed predominantly to particle loss. Loss of Si is from both soluble and particle loads. It is expected from soil chemistry at the

2D sites that both illite and chlorite dissolve congruently: therefore, during illite and chlorite dissolution, Mg, Si and K are released to solution while Al and Fe form secondary phases – kaolinite, Fe oxyhydroxides, Si–Al amorphous material, and Fe-coated primary materials – which are then lost as fine particles.

These “chemical” or “nonstoichiometric” weathering losses correlate to landscape position as indicated by the net elemental fluxes  $W_j$  illustrated in Fig. 7B. For example, the net fluxes of Mg,  $W_{Mg}$ , are  $0.2 \text{ g m}^{-2} \text{ y}^{-1}$  at the SPRT site,  $0.2 \text{ g m}^{-2} \text{ y}^{-1}$  at the SPMS site, and 0 at the SPVF site. A similar trend is observed for K at SPRT, SPMS, and SPVF:  $0.8 \text{ g m}^{-2} \text{ y}^{-1}$  to  $1.0 \text{ g m}^{-2} \text{ y}^{-1}$  to  $0 \text{ g m}^{-2} \text{ y}^{-1}$ , respectively. It has been suggested that geomorphic features (e.g., slope, soil thickness) can control chemical weathering reactions through availability of water (e.g., Lin et al., 2006; Burke et al., 2007). At the ridge top in SSHO, the chemical weathering is very intensive, presumably because a larger proportion of rainfall penetrates through the soil, moving downward to the bedrock instead of being lost through evapotranspiration (Graham et al., 1990). Furthermore, the soil waters in contact with minerals at the ridge top are expected to be dilute and far from chemical equilibrium. All these conditions favor faster reaction kinetics at the ridgetop. Consistent with these assumptions, the chemical weathering rates calculated at the middle slope site and ridge top are similar and higher than those calculated at the valley floor.

Consistent with these conclusions, the model yields negative chemical weathering rates for Si at the valley floor, indicating net accumulation instead of dissolution at that site for that element. As a secondary phase, kaolinite is observed at all three sites (Fig. 6D–F). We suggest that kaolinite particles are deposited or precipitated in the valley site. Net weathering losses of K and Mg are around zero at

the valley floor. Therefore, the solubilization of the primary minerals illite and chlorite is insignificant in the valley floor, as demonstrated by the similar CECs observed for SPVF soil and parent shale. In contrast, the CEC observed at the ridge top and middle slope sites are much lower, documenting loss of Mg during dissolution of chlorite and illite (SPRT and SPMS).

Overall dissolution of minerals near a ridge top and accumulation of major elements further along the flow path were also observed in a catena in New South Wales, Australia developed on granodiorite (Yoo et al., 2007). That transect, covered with soils whose average residence time was estimated as 1 ka, has a similar slope gradient but much higher CDF values ( $\sim 0.6$ ) compared to the transect here. As expected, granodiorite thus reacts faster than shale. Furthermore, in that system, subsurface translocation was not thought to be significant.

The model so far has been based upon the assumption of constant  $P$  with soil depth. In many cases,  $P$  has been inferred to vary with soil depth exponentially (e.g., Riebe et al., 2003; Heimsath et al., 2005). To investigate this possibility, we applied the same mass transport model as discussed above, but assumed that  $P$  decays as a function of soil thickness at different locations along the 2D transect:

$$p = p_0 e^{-\alpha h} \quad (25)$$

Here,  $\alpha$  is an empirical constant. We set this constant equal to  $0.022 \text{ cm}^{-1}$  following Heimsath et al. (2005), where  $h$  is soil thickness (cm).  $P_0$ , a reference soil production rate, is set equal to  $48 \text{ g m}^{-2} \text{ y}^{-1}$  by assuming  $P$  at the ridge top ( $h=30 \text{ cm}$ ) equals  $15 \text{ m/Myrs}$  ( $39 \text{ g m}^{-2} \text{ y}^{-1}$ ). For these assumptions, trends are observed to be similar to the previous depth-independent model (Table 5B and Fig. 7C, D), demonstrating that the major conclusions are consistent with either varying or non-varying  $P$ .

For both models, the net sediment fluxes ( $E$ ) decline from the ridge top to middle slope. Under the assumption of constant soil production rate,  $E$  values increase again at the valley floor site, becoming even higher at SPVF than at the ridge top. As seen in Fig. 1B, the transect is flat at the ridge and concave at the valley floor. The gentle slope at the valley floor should lead to lower net sediment flux, contradicting the model results. Therefore, the system is best described by the model where soil production rates vary with soil thickness: for that model,  $E$  at the valley floor is not as large as predicted for the other model.

#### 4.7. Mineral weathering rates

The calculated values of  $W_j$  for the SPRT site are essentially the extent of depletion of each element  $j$  divided by the residence time of the soil per unit geographical area. This rate can be converted to mineral surface-area based weathering rates ( $R$ , in mole mineral  $\text{m}^{-2} \text{ s}^{-1}$ ):

$$R = W_j / (M_j \rho S \beta h) \quad (26)$$

where  $M_j$  is atomic mass of element  $j$  (g/mol),  $\rho$  is bulk density ( $\text{g m}^{-3}$ ),  $S$  is specific surface area of the reacting mineral ( $\text{m}^2/\text{g}$ ) and  $\beta$  is the stoichiometric factor describing the number of atoms of element  $j$  in the reacting mineral formula.

The specific surface area, measured on SSHO soil samples (BA1 core in Fig. 1A) by nitrogen adsorption and the Brunauer–Emmett–Teller (BET) isotherm (Gregg and Sing, 1967), equals  $22\text{--}30 \text{ m}^2/\text{g}$ . This BET surface area value for bulk soil ( $\sim 25 \text{ m}^2/\text{g}$ ) was partitioned into illite and chlorite according to the mass ratio of these minerals (5:1). It was assumed that quartz did not contribute significantly because of its relatively low BET surface area (e.g., Klute, 1986). The mineral weathering rates for illite and chlorite calculated from Eq. (26) were then estimated at the ridge top from K and Mg data respectively after correcting for the appropriate stoichiometric factor:  $9 \times 10^{-17}$  and  $5 \times 10^{-17} \text{ mol m}^{-2} \text{ s}^{-1}$ .

These weathering rates are based on a calculation that is roughly equivalent to previous calculations based on mass balance used at other sites (Murphy et al., 1998; White, 2002; Brantley and White, 2009). Of course, in those previous approaches, the estimate of  $R$  was based on the observation of a gradient in the soil elemental profile measured for a ridgetop site that was interpreted to be at steady state. To implement that method following White (2002), we fitted our data at SPRT to a straight line, and these linear gradients were then used to derive mineral weathering rates for illite ( $2 \times 10^{-17} \text{ mol m}^{-2} \text{ s}^{-1}$ ) and chlorite ( $1 \times 10^{-17} \text{ mol m}^{-2} \text{ s}^{-1}$ ). These rates, like those discussed in the previous paragraph based on calculated values of  $W$ , are much slower than those from the laboratory. Indeed, for illite at the same pH conditions ( $\sim 4.5$ ), dissolution rates measured in laboratory experiments are much higher, varying from  $10^{-13.5}$  to  $10^{-14.5} \text{ mol m}^{-2} \text{ s}^{-1}$  (e.g., Kohler et al., 2005; Lowson et al., 2005). Such discrepancies between field and laboratory dissolution rates are common (White, 2008).

Incomplete depletion (i.e.,  $\tau$  not equal to  $-1$ ) at the land surface is observed for major elements and for the major minerals illite and chlorite. Depending on the relative contributions to the overall denudation from “chemical” weathering ( $W$ ,  $\text{g m}^{-2} \text{ y}^{-1}$ ) and physical erosion ( $E$ ,  $\text{g m}^{-2} \text{ y}^{-1}$ ), weathering systems have been in the past considered to be limited either by kinetics or transport (Stallard, 1992; West et al., 2005; Brantley and White, 2009; Lebedeva et al., 2010). In a transport-limited system, soils are relatively thick, reactive minerals tend to be leached completely from shallow horizons ( $\tau$  equals  $-1$ ), and the rate of denudation is limited by the rate of sediment transport out of the system. In kinetically limited systems, soils remain relatively thin, reactive minerals are not as highly leached near the surface, and the rate of denudation is limited by the rate of mineral dissolution. Based on the elemental profiles, carbonate weathering at SSHO is inferred to be transport-limited. In contrast, clay mineral profiles are controlled by slow dissolution kinetics, operating as a weathering-limited system (Lebedeva et al., 2010).

## 5. CONCLUSIONS

We studied weathering processes of the Rose Hill Formation at the SSHO with 25-m drill core samples and soils in sites located at ridgetops (“1D” sites where fluid flow is predominantly downward and thus one-dimensional) and on planar hillslopes (“2D” sites where flow of fluid and



sediment is predominantly two-dimensional downslope). The first weathering front where ankerite is dissolved may be as deep as 22 m below ground surface at the northern ridgetop. Shallower in the bedrock at this ridgetop site (~6 m), feldspar dissolution starts, followed by clay dissolution which initiates within the soil itself. Clay transformations during chemical weathering follow a complex pattern wherein the parent minerals illite and chlorite weather to vermiculite, HIV, and to kaolinite. Accompanying these transformations of mineralogy, Mg and K are released to streams as soluble loads and Al and Fe are transported through the subsurface as fine particles, especially as secondary kaolinite and Fe-oxyhydroxide. Both chemical weathering reactions and particle transport contribute to mass loss from the soils, forming depletion profiles for all major elements (Mg, K, Al, Fe, and Si). The incomplete depletion profiles of major elements and clay minerals are consistent with weathering limitation of these reactions, i.e., loss of Mg and K is controlled by slow mineral dissolution kinetics of clays (Stallard, 1992; Lebedeva et al., 2010).

A mass transport model applied to this transect is consistent with the inference that at ridge top and middle slope, chemical weathering can explain only about half of the elemental loss from the soils: the rest is lost by fine sediment transport throughout the soil profiles. However, chemical precipitation and/or physical accumulation are important at the valley floor due to transport from upslope. These model results are based upon an assumption that soils are maintained at steady state thickness, with a decrease of soil production rates from ridge top to valley floor along the 2D transect. This steady state assumption leads to no significant contradictions despite the fact that peri-glacial conditions 15 ky ago presumably accelerated erosion fluxes for some transient period.

The relatively limited number of major minerals present in the parent shale allows important observations to be made about weathering and erosion of this lithology. By emphasizing an investigation of 1D, 2D, and 3D sites on this monolithologic catchment, it is possible to constrain rates of weathering and erosion: ongoing research efforts on shales in other climate regimes are using similar approaches to enable comparison across climate. Other efforts should be pursued similarly on other lithologies to make lithologic comparisons as well.

#### ACKNOWLEDGMENTS

We thank those who helped with fieldwork, especially Z. Ruge, J. Flemming and J. Williams for sampling soil cores. We thank L. Liermann, H. Gong, M. Jungers, L. Reusser, A. Matmon, and R. Finkel for assistance in the lab. This work benefitted greatly from discussions with A. Blum, J. Peters, F. Pazzaglia, D. Eberl and the SSHO team, especially H. Lin, K. Singha, E. Kirby and R. Slingerland. Financial support is provided by National Science Foundation under Grant No. CHE-0431328 for Center for Environmental Kinetics Analysis and under Grant No. EAR-0725019 to Chris Duffy (PSU) for the Susquehanna/Shale Hills Critical Zone Observatory. Logistical support and/or data were provided by the NSF-supported Shale Hills Susquehanna Critical Zone Observatory. We thank Art White, Kyungsoo Yoo, and an anonymous reviewer for

constructive comments and Associate Editor Jon Chorover for handling of the manuscript.

#### APPENDIX A. SUPPLEMENTARY DATA

Supplementary data associated with this article can be found, in the online version, at [doi:10.1016/j.gca.2010.03.036](https://doi.org/10.1016/j.gca.2010.03.036).

#### REFERENCES

- Amacher M. C., Henderson R. E., Breithaupt M. D., Sele C. L. and LaBauve J. M. (1990) Unbuffered and buffered salt methods for exchangeable cations and effective cation-exchange capacity. *Soil Sci. Soc. Am. J.* **54**, 1036–1042.
- Amiotte-Suchet P., Probst J. L. and Ludwig W. (2003) Worldwide distribution of continental rock lithology: implications for the atmospheric/soil CO<sub>2</sub> uptake by continental weathering and alkalinity river transport to the oceans. *Global Biogeochem. Cycles* **17**, 1038. doi:10.1029/2002GB001891.
- Amundson, R. (2004) Soil formation. In *Treatise on Geochemistry* (eds. H. D. Holland and K.K. Turekian). Elsevier Press, Amsterdam, Chap. 5.01, pp. 1–35.
- Amundson R., Richter D. D., Humphreys G. S., Jobbage E. G. and Gaillardet J. (2007) Coupling between biota and earth materials in the Critical Zone. *Elements* **3**, 327–332.
- Anderson S. P., Dietrich W. E. and Brimhall G. H. (2002) Weathering profiles, mass-balance analysis, and rates of solute loss: linkage between weathering and erosion in a small, steep catchment. *Geol. Soc. Am. Bull.* **114**, 1143–1158.
- Anderson S. P., von Blanckenburg F. and White A. F. (2007) Physical and chemical controls on the Critical Zone. *Elements* **3**, 315–319.
- Bain D. C., Mellor A., Robertson-Rintoul M. S. E. and Buckland S. T. (1993) Variations in weathering processes and rates with time in a chronosequence of soils from Glen Feshie, Scotland. *Geoderma* **57**, 275–293.
- Berner E. K. and Berner R. A. (1996) *Global Environment: Water, Air and Geochemical Cycles*. Prentice-Hall, Inc., Upper Saddle River, New Jersey, 07458.
- Bierman, P. R., Reusser, L. and Pavich, M. (2009) New ways of using an old isotopic system – meteoric 10-Be is back and ready to do geomorphology. *Geophys. Res. Abstracts*, **11**, EGU2009-0.
- Bierman, P. R., Jungers, M., Reusser, L. and Pavich, M. (2008) Look again: meteoric 10-Be is a useful tracer of hillslope and basin-scale process. *Geol. Soc. Am. Abstracts Program*. pp. 165–166.
- Bierman, P., Reusser, L., Sullivan, C., Duxbury, J., Jungers, M., Reuter, J., Larsen, J., Pavich, M. and Finkel, R. (2007) A geochronologic glimpse into how ancient mountain ranges erode. *Geol. Soc. Am. Abstracts Program*.
- Blackmer G. C., Omar G. I. and Gold D. P. (1994) Post-Alleghanian unroofing history of the Appalachian Basin, Pennsylvania, from apatite fission trace analysis and thermal models. *Tectonics* **13**, 1259–1276.
- Blake, G. R. and Hartge, K. H. (1986) Bulk density. *Methods of Soil Analysis, Part1-I, Physical and Mineralogical Methods*, Ch. 13, second ed. (ed. Arnold Klute). pp. 363–375.
- Brantley S. B. and White A. F. (2009) Approaches to modeling weathered regolith. *Rev. Mineral. Geochem.* **70**, 435–484.
- Brantley, S. B., White, T. S., White, A. F., Sparks, D., Richter, D., Prigitz, K., Derry, L., Chorover, J., Chadwick, O., April, R., Anderson, S. and Amundson, R. (2006) Frontiers in exploration

- tion of the Critical Zone: Report of a workshop sponsored by the National Science Foundation (NSF), October 24–26, 2005, Newark, DE. p. 30.
- Brantley S. B., Godhaber M. B. and Ragnarsdottir K. V. (2007) Crossing disciplines and scales to understand the Critical Zone. *Elements* **3**, 307–314.
- Brantley S. B., Banstra J., Moore J. and White A. F. (2008) Modelling chemical depletion profiles in regolith. *Geoderma* **145**, 494–504.
- Braun D. D. (1989) Glacial and periglacial erosion of the Appalachians. *Geomorphology* **2**, 233–256.
- Brimhall G. H. and Dietrich W. E. (1987) Constitutive mass balance relations between chemical composition, volume, density, porosity, and strain in metasomatic hydrochemical systems: results on weathering and pedogenesis. *Geochim. Cosmochim. Acta* **51**, 567–587.
- Burke B. C., Heimsath A. M. and White A. F. (2007) Coupling chemical weathering with soil production across soil-mantled landscapes. *Earth Surf. Proc. Land.* **32**, 853–873.
- Carter B. J. and Ciolkosz E. J. (1986) Sorting and thickness of waste mantle material on a sandstone spur in central Pennsylvania. *Catena* **13**, 241–256.
- Chadwick O. A., Brimhall G. H. and Hendricks D. M. (1990) From a black to a grey box – a mass balance interpretation of pedogenesis. *Geomorphology* **3**, 369–390.
- Chadwick O. A. and Chorover J. (2001) The chemistry of pedogenic thresholds. *Geoderma* **100**, 321–353.
- Chadwick O. A., Derry L. A., Vitousek P. M., Huebert B. M. and Hedin L. O. (1999) Changing sources of nutrients during four million years of ecosystem development. *Nature* **397**, 491–497.
- Ciolkosz E. J., Carter B. J., Hoover M. T., Counce R. C., Waltman W. J. and Dobos R. R. (1990) Genesis of soils and landscapes in the Ridge and Valley province of central Pennsylvania. *Geomorphology* **3**, 245–261.
- Clark G. M. and Ciolkosz E. J. (1988) Periglacial geomorphology of the Appalachian highlands and interior highlands south of the glacial border—a review. *Geomorphology* **1**, 191–220.
- Copard Y., Amiotte-Suchet P. and Di-Giovanni C. (2007) Storage and release of fossil organic carbon related to weathering of sedimentary rocks. *Earth Planet. Sci. Lett.* **258**, 345–357.
- Duffy C. J. and Cusumano J. M. (1998) A low-dimensional model for concentration-discharge in groundwater-stream systems. *Water Resour. Res.* **34**, 2235–2247.
- Eberl, D. D. (2003) User's guide to RockJock – a program for determining quantitative mineralogy from powder X-ray diffraction data. U.S. Geological Survey, Open-file Report 03-78.
- El-Farhan Y. H., DeNovio N. M., Herman J. S. and Hornberger G. M. (2000) Mobilization and transport of soil particles during infiltration experiments in an agricultural field, Shenandoah Valley, Virginia. *Environmental Science & Technology* **34**, 3555–3559.
- Fernandes N. F. and Dietrich W. E. (1997) Hillslope evolution by diffusive processes: the timescale for equilibrium adjustments. *Water Resour. Res.* **33**, 1307–1318.
- Folk R. L. (1960) Petrography and origin of the Tuscarora, Rose Hill, and Keefer formations, Lower and Middle Silurian of eastern west Virginia. *J. Sed. Petrol.* **30**, 1–58.
- Gaillardet J., Dupré B., Louvat P. and Allègre C. J. (1999) Global silicate weathering and CO<sub>2</sub> consumption rates deduced from the chemistry of large rivers. *Chem. Geol.* **159**, 3–30.
- Gardner T. W., Ritter J. B., Shuman C. A., Bell J. C., Sasowsky K. C. and Pinter N. (1991) A periglacial stratified slope deposit in the valley and ridge province of central Pennsylvania, USA: sedimentology, stratigraphy, and geomorphic evolution. *Permafrost Periglac. Process.* **2**, 141–162.
- Graham R. C., Weed S. B., Bowen L. H., Amarasiwardena D. D. and Buol S. W. (1989) Weathering of iron-bearing minerals in soils and saprolite on the North Carolina Blue Ridge front: II. Clay mineralogy. *Clay Clay Mineral.* **37**, 29–40.
- Graham R. C., Daniels R. B. and Buol S. W. (1990) Soil-geomorphic relations on the Blue Ridge front: I. Regolith types and slope processes. *Soil Sci. Soc. Am. J.* **54**, 1362–1367.
- Green E. G., Dietrich W. E. and Banfield J. F. (2006) Quantification of chemical weathering rates across an actively eroding hillslope. *Earth Planet. Sci. Lett.* **242**, 155–169.
- Gregg S. J. and Sing K. S. W. (1967) *Adsorption, Surface Area and Porosity*. Academic Press, London, p. 370.
- Heimsath A. M., Furbish D. J. and Dietrich W. E. (2005) The illusion of diffusion: field evidence for depth dependent sediment transport. *Geology* **33**, 949–952.
- Helgeson H. C., Garrels R. M. and Mackenzie F. T. (1969) Evaluation of irreversible reaction in geochemical processes involving minerals and aqueous solutions II: applications. *Geochim. Cosmochim. Acta* **33**, 455–482.
- Hoskins, D. M. (1976) Pine Grove Mills Quadrangle Pennsylvania (7.5 min series, topographic). This map is from Map 61 – Atlas of Preliminary Geologic Quadrangle maps of Pennsylvania 1981, PA Geological Survey.
- Hseu Z. Y., Tsai H., Hsi H. C. and Chen Y. C. (2007) Weathering sequences of clay minerals in soils along a serpentinitic toposequence. *Clay Clay Miner.* **55**, 389–401.
- Jacobson A. D., Blum J. D., Chamberlain C. P., Craw D. and Koons P. O. (2003) Climatic and tectonic controls on chemical weathering in the New Zealand Southern Alps. *Geochim. Cosmochim. Acta* **67**, 29–46.
- Jin L., Hamilton S. K. and Walter L. M. (2008) Mineral weathering rates in glacial drift soils (SW Michigan, USA): new constraints from seasonal sampling of waters and gases at soil monoliths. *Chem. Geol.* **249**, 129–154.
- Kaplan I., Bertsch P. M. and Adriano D. C. (1997) Mineralogical and physicochemical differences between mobile and nonmobile colloidal phase in reconstructed pedons. *Soil Sci. Soc. Am. J.* **61**, 641–649.
- Kaste J. M., Heimsath A. M. and Bostick B. C. (2007) Short-term mixing quantified with fallout radionuclides. *Geology* **35**(3), 234–246.
- Klute, A. (1986) Methods of Soil Analysis. *Part I: Physical and Mineralogical Methods*, second ed. *SSSA Book Series 9* (Part 1). Soil Science Society of America, Madison, Wisconsin.
- Kohler S. J., Bosbach D. and Oelkers E. H. (2005) Do clay mineral dissolution rates reach steady state? *Geochim. Cosmochim. Acta* **69**, 1997–2006.
- Kolowitz L. C. and Berner R. A. (2002) Weathering of phosphorus in black shales. *Global Biogeochem. Cycles* **16**, 1140. doi:10.1029/2001GB001887.
- Kudrat M., Varadachari C. and Ghosh K. (2000) Application of the improved regression method to derive  $\Delta G$  of non-stoichiometric clay minerals and their correlations with compositional parameters. *Chem. Geol.* **168**, 225–238.
- Kurtz A. C., Derry L. A., Chadwick O. A. and Alfano M. J. (2000) Reflectory element mobility in volcanic soils. *Geology* **28**, 683–686.
- Laegdsmand M., Villholth K. G., Ullum M. and Jensen K. H. (1999) Processes of colloid mobilization and transport in macroporous soil monoliths. *Geoderma* **93**, 33–59.
- Lebedeva M. I., Fletcher R. C. and Brantley S. L. (2010) A mathematical model for steady-state regolith production at constant erosion rate. *Earth Surf. Proc. Land.* **35**, 508–524.
- Lee B. D., Sears S. K., Graham R. C., Amrhein C. and Vali H. (2003) Secondary mineral genesis from chlorite and serpentine

- in an ultramafic soil toposequence. *Soil Sci. Soc. Am. J.* **67**, 1309–1317.
- Lin H. S. (2006) Temporal stability of soil moisture spatial pattern and subsurface preferential flow pathways in the Shale Hills Catchment. *Vadose Zone J.* **5**, 317–340.
- Lin H., Kogelmann W., Walker C. and Bruns M. A. (2006) Soil moisture patterns in a forested catchment: a hydrogeological perspective. *Geoderma* **131**, 345–368.
- Lin H. and Zhou X. (2008) Evidence of subsurface preferential flow using soil hydrologic monitoring in the Shale Hills catchment. *Eur. J. Soil Sci.* **59**, 34–49.
- Litke R., Klusmann U., Krooss B. and Leythaeuser D. (1991) Quantification of loss of calcite, pyrite, and organic matter due to weathering of Toarcian black shales and effects on kerogen and bitumen characteristics. *Geochim. Cosmochim. Acta* **55**, 3369–3378.
- Lowson R. T., Comarmond M.-C. J., Rajaratnam G. and Brown P. L. (2005) The kinetics of dissolution of chlorite as a function of pH and at 25 °C. *Geochim. Cosmochim. Acta* **69**, 1687–1699.
- Lynch J. A. and Corbett E. S. (1985) Source-area variability during peak flow. In *Drain. Div. Am. Soc. Civ. Eng.* (eds. E. B. Jones, T. J. Ward and J. Irrig) (eds. E. Jones and T. Ward). ASCE, Reston, VA, pp. 300–307.
- Lynch, J. A. (1976) Effects of antecedent soil moisture on storm hydrographs. PhD Dissertation. Pennsylvania State University, University Park, PA.
- Moore, M. D. and Reynolds, Jr., C. R. (1997) *X-Ray Diffraction and the Identification and Analysis of Clay Minerals*, second ed. Oxford University Press, Oxford, New York.
- Murphy S. F., Brantley S. L., Blum A. E., White A. F. and Dong H. (1998) Chemical weathering in a tropical watershed, Luquillo Mountains, Puerto Rico: II. Rate and mechanism of biotite weathering. *Geochim. Cosmochim. Acta* **62**, 227–244.
- National Oceanographic and Atmospheric Administration (NOAA) (2007) U.S. divisional and station climatic data and normals: Asheville, North Carolina, U.S. Department of Commerce, National Oceanic and Atmospheric Administration, National Environmental Satellite Data and Information Service, National Climatic Data Center. <http://cdo.ncdc.noaa.gov/CDO/cdo>.
- Neaman A., Chorover J. and Brantley S. L. (2006) Effects of organic ligands on granite dissolution in batch experiments at pH 6. *Am. J. Sci.* **306**, 451–473.
- Petsch S. T., Eglinton T. I. and Edwards K. J. (2001) 14C-dead living biomass: evidence for microbial assimilation of ancient organic carbon during shale weathering. *Science* **292**, 1127–1131.
- Piersson-Wickmann A., Reisberg L. and France-Lanord C. (2002) Behavior of Re and Os during low-temperature alteration: results from Himalayan soils and altered black shales. *Geochim. Cosmochim. Acta* **66**, 1539–1548.
- Poppe, L. J., Paskevich, V. F., Hathaway, J. C. and Blackwood, D. S. (2002) A laboratory manual for X-ray powder diffraction. U.S. Geological Survey Open File Report 01–041. U.S. Geological Survey, MA.
- Price J. R., Velbel M. A. and Patino L. C. (2005) Rates and time scales of clay–mineral formation by weathering in saprolitic regoliths of the southern Appalachians from geochemical mass balance. *Geol. Soc. Am. Bull.* **117**, 783–794.
- Qu Y. and Duffy C. J. (2007) A semidiscrete finite volume formation for multiprocess watershed simulation. *Water Resour. Res.* **43**. doi:10.1029/2006WR005753.
- Reuter, J., Bierman, P., Pavich, M., Gellis, A., Larsen, J. and Finkel, R. (2004) Erosion of the Susquehanna River Basin: assessing relations between <sup>10</sup>Be-derived erosion rates and basin characteristics. *Geol. Soc. Am. Program. Abstracts*.
- Riebe C. S., Kirchner J. W. and Finkel R. C. (2003) Long-term rates of chemical weathering and physical erosion from cosmogenic nuclides and geochemical mass balance. *Geochim. Cosmochim. Acta* **67**, 4411–4427.
- Roering J. J., Kirchner J. W. and Dietrich W. E. (2001) Hillslope evolution by nonlinear, slope-dependent transport: steady-state morphology and equilibrium adjustment timescales. *J. Geophys. Res.* **106**, 16499–16514.
- Roden M. K. and Miller D. S. (1989) Apatite fission-track thermochronology of the Pennsylvania Appalachian Basin. *Geomorphology* **2**, 39–51.
- Rose, A.W. (1973) Structure and Silurian and Devonian stratigraphy of the Valley and Ridge Province in Central Pennsylvania. In *The 38th Annual Field Conference of Pennsylvania Geologists*.
- Rousseau M., Di Pietro L., Angulo-Jaramillo R., Tessier D. and Cabibel B. (2004) Preferential transport of soil colloidal particles: physicochemical effects on particle mobilization. *Vadose Zone J.* **3**, 247–261.
- Sevon, W. D. and Braun, D. D. (1997) Glacial deposits of Pennsylvania map. Bureau of Topographic and Geological Survey, Department of Conservation and Natural Resources, Map 59, second ed.
- Stallard, R.F. (1992) Tectonic processes, continental freeboard, and the rate-controlling step for continental denudation. In *Global Biogeochemical Cycles* (eds. S. S. Butcher, R. J. Charlson, G. H. Orians, G. V. Wolfe). Academic Press, London, pp. 93–121.
- Stone, J. (1998) A rapid fusion method for separation of beryllium-10 from soils and silicates. *Geochim. Cosmochim. Acta* **62**, 555–561.
- Taylor A. and Blum J. D. (1995) Relation between soil age and silicate weathering rates determined from the chemical evolution of a glacial chronosequence. *Geology* **23**, 979–982.
- Taylor A. and Velbel M. A. (1991) Geochemical mass balances and weathering rates in forested watersheds of the southern Blue Ridge II. Effects of botanical uptake terms. *Geoderma* **51**, 29–50.
- United States Department of Agriculture, Natural Resources Conservation Service (2004). Soil survey laboratory methods manual. Version No. 4.0. Soil Survey Investigations Report No. 42.
- West A. J., Galy A. and Bickle M. (2005) Tectonic and climatic controls on silicate weathering. *Earth Planet. Sci. Lett.* **235**, 211–228.
- White A. F. (2002) Determining mineral weathering rates based on solid and solute weathering gradients: application to biotite weathering in saprolites. *Chem. Geol.* **190**, 69–89.
- White A. F. (2008) Quantitative approaches to characterizing natural chemical weathering rates. In *Kinetics of Water-Rock Interaction* (eds. S. L. Brantley, J. D. Kubicki and A. F. White). Springer, New York, pp. 469–544.
- White A. F. and Blum A. E. (1995) Effects of climate on chemical weathering in watersheds. *Geochim. Cosmochim. Acta* **59**, 1729–1747.
- White A. F., Blum A. E., Marjorie S., Schulz M. S., Bullen T. D., Harden J. W. and Peterson M. L. (1996) Chemical weathering rates of a soil chronosequence on granitic alluvium: I. Quantification of mineralogical and surface area changes and calculation of primary silicate reaction rates. *Geochim. Cosmochim. Acta* **60**, 2533–2550.
- White A. F., Bullen T. D., Vivit D. V., Schulz M. S. and Clow D. W. (1999) The role of disseminated calcite in the chemical weathering of granitoid rocks. *Geochim. Cosmochim. Acta* **63**, 1939–1953.

- White A. F., Bullen T. D., Schulz M. S., Blum A. E., Huntington T. G. and Peters N. E. (2001) Differential rates of feldspar weathering in granitic regoliths. *Geochim. Cosmochim. Acta* **65**, 847–869.
- White A. F., Schulz M. S., Vivit D. V., Blum A. E., Stonestrom D. A. and Harden J. W. (2005) Chemical weathering rates of a soil chrono-sequence on granitic alluvium: III. Hydrochemical evolution and contemporary solute fluxes and rates. *Geochim. Cosmochim. Acta* **69**, 1975–1996.
- White A. F., Schulz M. S., Vivit D. V., Blum A. E., Stonestrom D. A. and Anderson S. P. (2008) Chemical weathering of a marine terrace chronosequence, Santa Cruz, California I: interpreting rates and controls on soil concentration-depth profiles. *Geochim. Cosmochim. Acta* **72**, 36–68.
- White, G. N. and Dixon, J. B. (2003) *Soil Mineralogy Laboratory Manual, ninth ed. Department of Soil and Crop Sciences*. Texas A&M University, College Station, TX77843.
- Williams E. L., Szramek K. J., Jin L., Ku T. C. W. and Walter L. M. (2007) The carbonate system geochemistry of shallow ground water–surface water systems in temperate glaciated watersheds (Michigan, USA): significance of open-system dolomite weathering. *Geol. Soc. Am. Bull.* **119**, 515–528.
- Wilson M. J. (2004) Weathering of primary rock forming minerals: processes, products, and rates. *Clay Mineral.* **39**, 233–266.
- Yoo K., Amundson R., Heimsath A. M., Dietrich W. E. and Brimhall G. H. (2007) Integration of geochemical mass balance with sediment transport to calculate rates of soil chemical weathering and transport on hillslopes. *J. Geophys. Res.* **112**, F02013. doi:10.1029/2005JF000402.

Associate editor: Jon Chorover